Experiments on secondary instability of streamwise vortices in a swept-wing boundary layer

By VALERY G. CHERNORAY[1], ALEXANDER V. DOVGAL[2], VICTOR V. KOZLOV[2] AND LENNART LÖFDAHL[1]

[1]Applied Mechanics, Chalmers University of Technology, SE-412 96 Göteborg, Sweden
[2]Institute of Theoretical and Applied Mechanics, 630090 Novosibirsk, Russia

A detailed experimental study on the formation of crossflow vortex mode packets and their high-frequency secondary instability in a swept-wing boundary layer was carried out. Stationary vortex packets are most likely to be generated under natural flight conditions and transition to turbulence is quickest within these disturbances. In the present experiments, different methods of controlled excitation are used so that the crossflow vortex packets are generated by surface-roughness elements and by localized continuous suction. It is found that as the stationary disturbance reaches a significant amplitude, of about 10% of the free-stream velocity, while being below the saturation level, high-frequency secondary instabilities start to grow. Influence of the crossflow vortex packet magnitude on the development of the secondary instability is investigated in detail and below its threshold the crossflow vortex packet was found to be nearly neutrally stable. By studying the unstable packets, the frequency of natural secondary perturbations was identified and the travelling disturbances were forced in a controlled manner by periodic blowing–suction applied locally under the stationary vortex. Two modes of secondary instability were found to develop and the preferred mode was dependent on the properties of the primary stationary disturbance. Additionally, the underlying physics of the process of nonlinear formation and development of the vortices in the boundary layer is clarified. It was observed that the large-amplitude co-rotating vortices may interact, thus reducing their amplitude. Also a large-scale excitation by an isolated roughness element produced two individual stationary crossflow vortex packets at its tips, each with different preferred secondary instability modes.

1. Introduction

There are a number of indications that three-dimensional velocity perturbations such as streamwise vortices and streaks are involved in transition to turbulence in wall-bounded shear layers. Creating local flow distortions, they induce velocity gradients in spanwise and wall-normal directions, which in turn lead to the growth of secondary high-frequency disturbances with further laminar-flow breakdown. This transitional phenomenon seems to be general for different configurations (Kohama *et al.* 2000) including a flat-plate boundary layer (Matsubara & Alfredsson 2001), a three-dimensional one (Kohama, Onodera & Egami 1996), a plane Poiseuille flow (Elofsson, Kawakami & Alfredsson 1999), a flow in a rotating curved channel

(Matsson & Alfredsson 1990) and that over a concave wall (Ito 1988). It can be noted that similar processes are distinguished in near-wall turbulence as was shown by Schoppa & Hussain (2002).

Secondary instabilities of three-dimensional boundary layers were at first focused on by Poll (1979, 1985), who observed high-frequency oscillations near the swept-wing leading edge and on a swept cylinder. Later, Kohama (1987) assumed that such perturbations can be caused by an inflection-point instability in the vortex core. A theory for the secondary disturbances, such as those associated with inflections in the velocity distributions induced by the stationary crossflow vortices, was developed further by Fischer & Dallmann (1991) who used experimental results by Nitschke-Kowsky & Bippes (1988) as initial data for the analysis based on the Floquet theory. Then, theoretical studies on the topic were carried out by Malik, Li & Chang (1994), Malik *et al.* (1999), Haynes & Reed (1997, 2000), Janke & Balakumar (2000) and Koch *et al.* (2000), where the Floquet theory was employed as a basis for temporal secondary instability analysis. To simplify the problem, which involves a number of parameters, Koch *et al.* (2000) investigated equilibrium solutions, which were independent of the initial conditions, and in a more recent study Koch (2002), using the saddle-point continuation method, found that the wave packets of high-frequency secondary disturbances are convectively unstable. In fact, he has pointed out that one can approach the problem by a spatial marching technique such as parabolized stability equations. Saric, Reed & White (2003) provide a detailed review of recent studies in this field.

The first spatial direct numerical simulation of the swept-wing secondary instability, applying to the Falkner–Skan–Cooke similarity solution, was performed by Högberg & Henningson (1998). They examined both a small-amplitude random ('natural') disturbance added to a saturated crossflow vortex and its harmonic perturbation. It was found that the growth rate of the high-frequency secondary disturbance is considerably larger than that of the low-frequency one, thus, the importance of high-frequency secondary instabilities for laminar-flow breakdown was emphasized. Wassermann & Kloker (2002) also performed spatial direct numerical simulation focusing on an infinite swept-wing flow. In their case, secondary instabilities induced by the saturated crossflow vortices were investigated, their convective nature was confirmed and conditions for the instability onset were considered. Additionally, they demonstrated that saturated uniform crossflow vortices initiated by a single crossflow vortex mode are less unstable than those produced by a packet of modes. Also, it was found that reduction of spacing between the saturated vortices leads to stabilization of the modulated boundary layer.

To support the results of calculations and to deepen understanding of the phenomenon a number of experimental studies have been carried out. Kohama, Saric & Hoos (1991) emphasized that the high-frequency secondary instabilities originate in regions of strong vorticity and shear away from the wall at about half the boundary-layer thickness. Kohama *et al.* (1996) presented results on the amplification of the secondary modes from a swept flat-plate experiment. Deyhle & Bippes (1996) also focused on a high-frequency disturbance riding on top of the primary waves prior to a local breakdown to turbulence.

In a series of wind-tunnel experiments, different techniques of controlled disturbance excitation, applied to the primary steady and secondary unsteady instabilities, were used successfully. Using this technique, Kawakami, Kohama & Okutsu (1999) obtained growth curves and amplitude distributions of the secondary perturbations. Boiko *et al.* (1995*a*,*b*, 1998, 2000) investigated different aspects of the problem experimentally. It

was shown that the amount of secondary instability depends on how the primary vortices are generated and on their spanwise spacing. In Boiko *et al.* (2000), it was also noticed that packets of stationary crossflow modes are more unstable as compared to single-mode crossflow vortices. Additionally, linearity of the travelling disturbances at the initial stage of their amplification was confirmed and a local instability mechanism associated with velocity gradients induced by the primary vortices was supported. White *et al.* (2001) and White & Saric (2005) reported results obtained under different initial steady conditions, focusing on two major types of high-frequency secondary instability modes. These are a '*y*' mode and a '*z*' mode, which are analogous to a symmetric (also horseshoe, varicose) mode and an anti-symmetric (meandering, sinuous) mode of two-dimensional flows modulated by streaks. White *et al.* and White & Saric excited the primary stationary modes artificially, while the secondary instabilities under investigation occurred naturally. Authors have used band-pass filtering to separate different high-frequency secondary instability modes. Extensive studies of these modes have been performed experimentally (Asai, Minagawa & Nishioka 2002; Chang, Chernoray & Löfdahl 2003; Kozlov *et al.* 2004) as well as numerically (Andersson *et al.* 2001; Schoppa & Hussain 2002; Brandt & Henningson 2002; Skote, Haritonidis & Henningson 2002) in two-dimensional flows. The '*z*' mode was found to dominate when the primary vortex wavelength was short and the '*y*' mode dominated when the vortex spacing was large. Thus, it was concluded that the most important factor for the secondary instability is the wavelength of the stationary perturbations.

Under natural conditions of wing flow transition, packets of stationary crossflow vortex modes, rather than single-mode vortices, develop in the boundary layer. Furthermore, recent studies show that secondary instabilities develop in a different way on the vortex packets than on the single-mode vortices. As was mentioned above, both calculations (Wassermann & Kloker 2002) and experiments (Boiko *et al.* 2000) show higher instability of packets of stationary crossflow modes as compared to single crossflow vortex modes, hence, a lower limit for secondary instability can be obtained through a consideration of the stability of such packets. The stability properties of crossflow vortex packets is investigated in some detail by Wassermann & Kloker (2002) and in experiments by Kozlov, Sova & Shcherbakov (2001), however, a deeper understanding is needed. Moreover, there are some indications that for crossflow vortices it is not absolutely required to reach a saturation state for a secondary instability to start to grow. This can be observed from the measurement data of Boiko *et al.* (1997) and from the secondary instability analysis of Malik *et al.* (1999). Thus, unsaturated vortices may lead to laminar-flow breakdown and this issue requires additional investigation.

To complement the above data on secondary instabilities in swept-wing boundary layers, the present experiments were designed with the idea of modelling the phenomenon under fully controlled conditions. In this work, which uses an experimental set-up similar to that of Boiko *et al.* (2000), the '*y*' and '*z*' high-frequency secondary instability modes of various packets of stationary crossflow vortex modes are investigated both separately and at their interaction. In particular, this is performed with an implication to the transition prediction and control in three-dimensional boundary layers. According to White *et al.* (2001) and Saric *et al.* (2003), the location of secondary instability onset can be used as the transition location, and the investigation of factors responsible for the instability onset is crucial in establishing the transition prediction and control criteria. In our case, to resolve the secondary disturbances as much as possible, a method of hot-wire visualization is employed, and quantitatively resolved flow topology is also given. Thus, wind-tunnel results presented
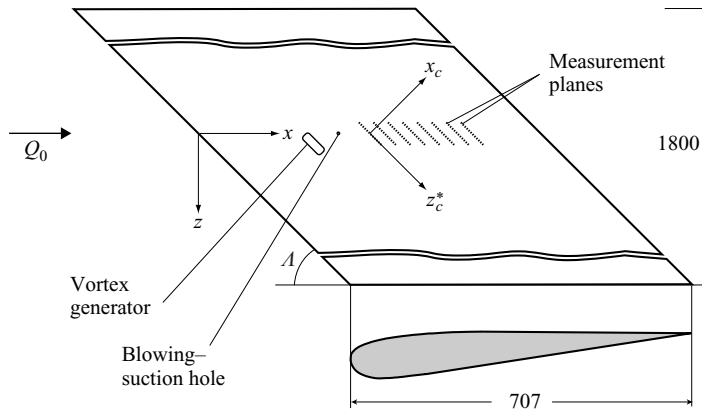
FIGURE 1. The swept-wing model. Chordwise (x_c, z_c^*) and wind-tunnel-related (x, z) coordinate systems are shown. Dimensions are in mm.

in what follows provide in great detail the three-dimensional flow characteristics as was accomplished before for the two-dimensional boundary layer by Asai *et al.* (2002).

2. Experimental set-up and procedure

All experiments were conducted at Thermo and Fluid Dynamics, Chalmers University of Technology. The wind tunnel has a closed circuit and a test section 3 m long, 1.8 m wide and 1.2 m high with a maximum velocity of $60 \, \mathrm{m \, s^{-1}}$. A detailed description of the facility is provided by Chernoray *et al.* (2005). The free-stream turbulence level in the test section is well below 0.1 % of Q_0 in the velocity range of $Q_0 = 5$–$15 \, \mathrm{m \, s^{-1}}$ at frequencies between 0.1 and 10 000 Hz. The flow temperature can be controlled with a precision of $\pm 0.1 \, ^\circ\mathrm{C}$. Velocity in the wind tunnel was monitored using a Pitot-static tube connected to a digital micro-manometer, which also has sensors for temperature and absolute pressure readings. All the experimental runs discussed in what follows were performed with an oncoming flow velocity of $8.2 \, \mathrm{m \, s^{-1}}$, making the chord-based Reynolds number about 390 000.

The wing model is made of wood and has a C-16 aerofoil profile as depicted in figure 1, which was positioned at the sweep angle, Λ, of 45°. Chord length, c, in this configuration of sweep was 707 mm and the chord as measured perpendicular to the wing leading edge, c_c, is 500 mm. The model spanned the entire width of the wind-tunnel test section. As can be seen in figure 1, the top side of the wing after 0.4 chord represents a flat surface, thus allowing study of the flow without the presence of a wall-curvature effects. The wing was mounted horizontally in the middle of the test section on a stand extending outside the wind tunnel. Using this stand the angle of attack and height of the model could be altered. For the purpose of this experiment, the angle of attack was chosen so that no separation occurred in the area of measurements, after 0.3 chord. This condition was satisfied when the top flat surface of the wing created a diffuser and was angled from the horizon at approximately 2°. A sandpaper strip was placed close to the leading edge on the bottom side of the model to prevent large-scale separation and to avoid associated global unsteadiness of the flow.

Two coordinate systems, i.e. wind-tunnel-related (x, z) and wing-related (x_c, z_c), are also depicted in figure 1. The wing-related coordinate system is such that x_c lies perpendicular to the wing leading edge and z_c is in the spanwise direction. Since the angle of incidence of the top wing surface was fairly small (2°), it is assumed

that the y-axes of the wind-tunnel-related coordinate system and the wing-related coordinate system are coincident, thereby simplifying the measurements. To compare experimental and theoretical velocity profiles, some results are depicted in the frame of reference of the external flow streamline, using the coordinate system (x_s, z_s).

All the data were acquired from hot-wire measurements in z slices along the leading edge of the wing, as shown in figure 1. Single cross-planes are represented as they were measured in the wing-related coordinate system. However, for clarity, the axis z_c in the graphs is shifted so that its origin is coincident with the origin of the wind-tunnel-related coordinate system. For a sweep angle of $45°$, the transformation is as follows:

$$z_c^* = z_c - x_c \tan \Lambda = z_c - x_c. \tag{2.1}$$

This allows the origin of the z_c^*-axis to be in-line with the blowing–suction hole as depicted in figure 1.

Stationary crossflow vortices were generated in the laminar boundary layer by roughness elements or by localized continuous suction. The perturbation of the layer was performed at 0.3 of the wing chord, see figure 1. The procedure of the vortex generation and experimental configurations are described in more detail in §3.2.

High-frequency travelling disturbances evolving along the streaks were excited by periodic blowing–suction through a hole of 0.8 mm in diameter on the surface of the model at 0.4 chord. The oscillations were produced by a loudspeaker and the excitation frequency was 210 Hz. This frequency is close to the one which is most amplified naturally for different types of instability modes.

The velocity data was obtained through hot-wire measurements by single and V-wire probes. The hot wires were calibrated in the free stream versus the Pitot-static tube. Details on the experimental procedure as well as on the measurement equipment used can be found in Chernoray *et al.* (2005). Typically, the calibration resulted in an error of less than 0.5 % for all points in the calibration range. A unique hot-wire traversing mechanism was developed, which is computer controlled and can be completely automated for long experimental runs through definition of a geometrical mesh of measurement points. Equipped with servo-motors it can sustain an absolute coordinate system with an accuracy of 10 μm in the x and z directions, and 5 μm in y direction. The acquisition system is the IOTech Wavebook 516 sampling module with expansion unit, enabling a 16-bit, 1 MHz sample and hold with full analogue and digital triggering options. The software used to control the sampling and saving of data files is linked into a program for automated triggered flow measurements using the traversing system and a pre-defined mesh of sampling points. Using this high-precision equipment and a fully automated experimental procedure, it was possible to obtain detailed experimental data.

After the data were collected, post-processing was carried out in the software package Matlab (Matrix Laboratory, USA). Voltage traces were converted to velocity traces and phase averaged to give a single period of the oscillation. These are then assembled to form a four-dimensional spatial and temporal matrix $U(x, y, z, t)$. For the spectral analysis either raw or ensemble-averaged velocity traces were used.

3. Results and discussion

3.1. *Basic flow*

Without the excitation of disturbances, a typical laminar flow was formed on the top surface of the wing, which had an initial region of acceleration followed by
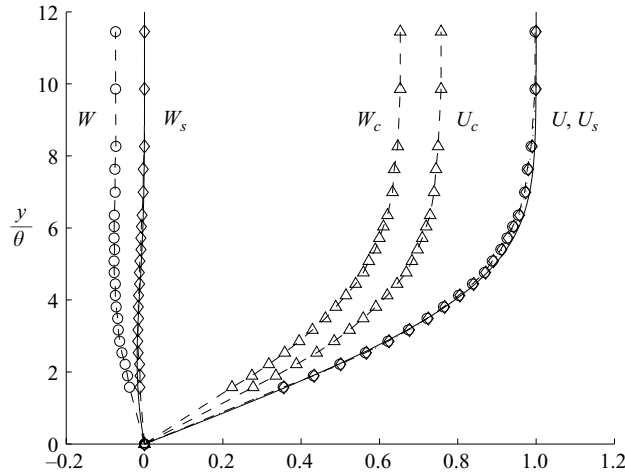
FIGURE 2. Undisturbed non-dimensional (scaled by Q_e) velocity profiles measured at the station $x/c = x_c/c_c = 0.3$, where the roughness element is placed. Profiles of streamwise and spanwise velocity components are shown in different coordinate systems; $\theta = 0.31$ mm at this station. Solid lines indicate Falkner–Skan–Cooke similarity solution for $m = 0.04$ and $\phi = 40.8°$; dashed lines are guiding through the experimental points.

an area of flow deceleration. Velocity profiles obtained at 0.3 chord, where the roughness element was located, are demonstrated in figure 2. The profiles are shown in different coordinate systems: wind-tunnel-related (x, z), wing-related (x_c, z_c) and external streamline-related (x_s, z_s). The wall-normal coordinate, y, in this figure and everywhere in what follows is scaled by the boundary-layer momentum thickness, θ, which is defined using only the streamwise velocity component, U_s. As can be seen, the basic flow in this station is approximated well by the Falkner–Skan–Cooke similarity solution for an accelerated boundary layer with an external streamline angle ϕ equal to 40.8°, which corresponds to the local external flow angle at this station.

Owing to the continuous deceleration of the potential flow downstream of 0.3 chord, the boundary-layer properties are changed. Downstream of 0.5 chord, a nearly self-similar Falkner–Skan–Cooke boundary layer is formed with $m = -0.05$. Figure 3(a, b) demonstrates good agreement of the external velocity variation and of the integral boundary layer parameters with the theoretical prediction. In this figure, the shape factor, H_{12}, is defined as the ratio of boundary-layer displacement thickness to momentum thickness. The theoretical shape factor is 2.71 and as can be seen, a minor scatter of measurements around the theoretical value exists with little deviation and the flow is nearly perfectly uniform. The theoretical variation of external velocity and boundary-layer momentum thickness is as follows:

$$U_{ce} = Q_0 \cos \Lambda x_c^{-0.05}, \tag{3.1}$$

$$W_{ce} = Q_0 \sin \Lambda, \tag{3.2}$$

$$\theta = \Theta \left(\frac{\nu x^*}{Q_e} \right)^{1/2}, \tag{3.3}$$

where x^* is the streamwise coordinate x shifted by the origin of the virtual leading edge (0.1 m) and $\Theta = 0.741$ is the non-dimensional momentum thickness of the Falkner–Skan–Cooke boundary layer, see Corbett & Bottaro (2001) for details.
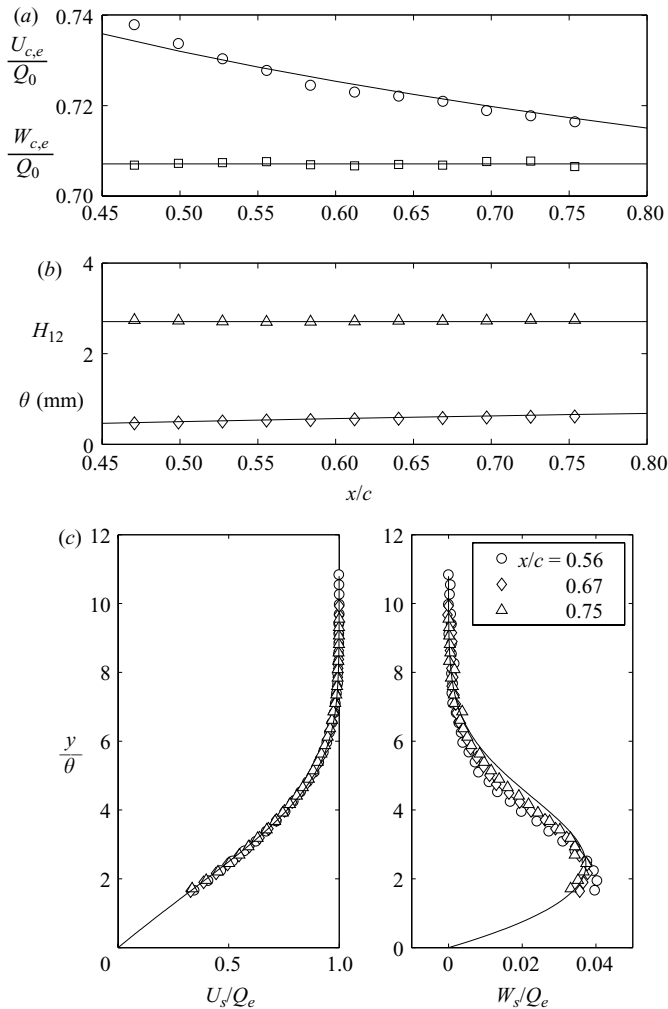
FIGURE 3. (*a*) Downstream distribution of streamwise, U_c ($\circ$) and spanwise, W_c ($\square$) potential flow velocity components; (*b*) distribution of boundary-layer displacement thickness, θ ($\diamond$), and shape factor, H_{12} ($\triangle$); (*c*) profiles of streamwise U_s and spanwise W_s velocity in coordinate system of external flow streamline. In all graphs lines denote theory for $m = -0.05$.

Mean velocity profiles for different streamwise positions within 0.47 to 0.75 wing chord were measured at the airfoil spanwise centreline, and some of them, corresponding to the range of subsequent transition measurements, are shown in figure 3(*c*). The illustrated velocity profiles are given in the external streamline coordinate system. Here, the similarity solution is obtained for $\phi = 44.3°$, which corresponds to the average external flow angle for the experimental profiles shown. In this figure, good collaboration between the data and the theoretical solution can be observed. Thus, a well-defined flow is obtained on the model with a characteristic Reynolds number, Re_θ, at the location of the roughness element, of about 175.

3.2. *Stationary crossflow vortex mode packets. Natural secondary instability*

During experiments, a packet of stationary vortex modes may be generated effectively either by a single roughness element or by localized continuous blowing/suction.
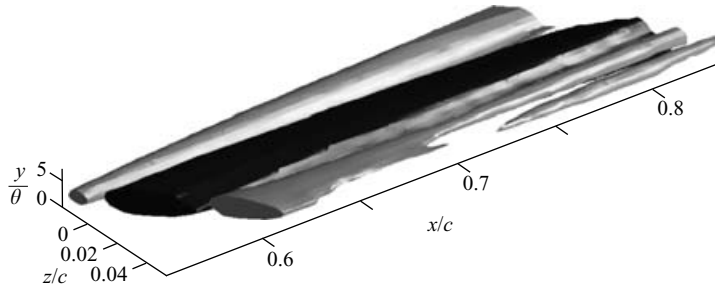
FIGURE 4. Isosurfaces of the stationary disturbance of streamwise velocity, U', due to the 35 mm long roughness element (light: $-6\,\%$, dark: $+6\,\%$ of Q_0).

Indeed, both methods are used in the current paper. To study secondary instabilities of such a vortex under controlled conditions, it is necessary for the vortex amplitude to be relatively large, otherwise random natural disturbances will cause the loss of synchronization, making triggered measurements impossible. Thus, it is necessary to generate strong vortices, which are therefore nonlinear. In addition, a combination of nonlinear receptivity and nonlinear stability causes the spanwise extent of the roughness element to be a crucial parameter of the vortex packet generation, as was mentioned by Boiko *et al.* (2000).

Experimentally, we found that the most effectively generated stationary crossflow mode has a spanwise wavelength of about 20 mm. Experiments by Boiko *et al.* (2000) were conducted at nearly the same conditions and they found that a vortex packet containing primarily this mode can be effectively generated using an isolated roughness element of about 35 mm spanwise width. In this case, behind a roughness element a pair of nearly independently developing vortices of opposite rotation and of necessary wavelength is generated. In figure 4, the mean velocity distortion created by such a roughness element is shown. Three distinct streaks are observed in the boundary layer: an area of velocity acceleration right behind the roughness element and two areas of velocity slow-down on the sides.

The three-dimensionality of the flow pattern of streamwise vortical structures makes their studies difficult. This is one of the reasons why the mechanism of streamwise vortical structure formation (at high free-stream turbulence level or behind a three-dimensional roughness element) is still unclear. Recently, a concept of the lift-up effect was proposed, see Boiko *et al.* (2002) for details, which is essentially useful for understanding of this issue. In particular, one can claim that the lift-up effect operates at the side edges of a three-dimensional roughness element and forms a pair of streaks. Additionally, for two-dimensional flows, a direct numerical simulation by Roget *et al.* (1998) is available. In this work, the development of disturbance behind a three-dimensional roughness element is concerned. Unfortunately, no such investigations exist for the case of a three-dimensional flow.

In our case, the process of formation of the streaks is illustrated by figure 5, where a slice at $x_c/c_c = 0.54$ taken along the leading edge of the wing is shown in detail. In figure 5(*a*), contours of mean streamwise velocity are shown and it can be seen that these are only slightly distorted and the vortices are far from saturation. Disturbance of the mean streamwise velocity is depicted in figure 5(*b*), where positive values of disturbance velocity are shown by solid lines and the dashed lines represent negative values. It is obvious that the disturbance lies deep inside the boundary layer, below $y/\theta = 8$. Crossflow velocity components are shown by arrows in figure 5(*c, d*).
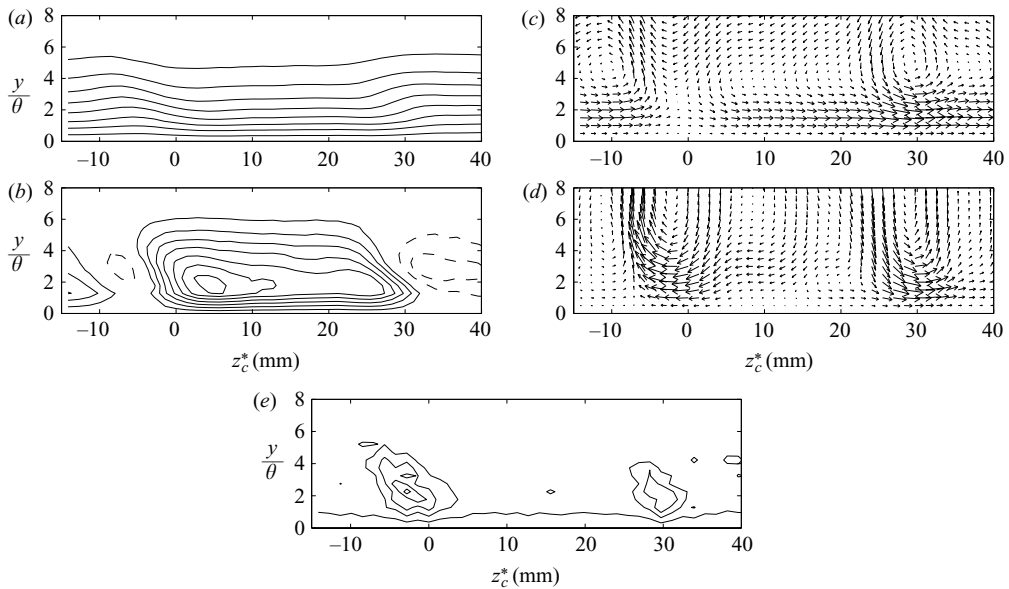
FIGURE 5. Mean velocity behind the 35 mm long roughness element at $x_c/c_c = 0.54$: (*a*) streamwise velocity, U, (*b*) disturbance of streamwise velocity, U', (*c*) crossflow velocity components and (*d*) disturbance of crossflow velocity. (*e*) naturally occurring secondary instabilities are shown by r.m.s. contours. Contour levels in (*a*): 0.1138, 0.2276,...,0.9103 of U_e; in (*b*): increment between contours is 0.2 of $\Delta U_{0.5}$, dashed lines used for negative values, solid lines for positive values, zero-level is not shown; levels in (*e*): 0.1784, 0.3568,...,0.8921 of $u'_{max(y,z)}$.

To obtain these graphs, two components, streamwise and spanwise velocity were measured by a V-probe, and wall-normal velocity is computed from integration of the continuity equation. In particular, figure 5(*d*) explains the formation of the streaks in the boundary layer. In this figure, it is seen that the crossflow vortex packet consists of a pair of counter-rotating vortices which form at the sides of the roughness element and seem to be sufficiently separated from each other to develop without significant interaction. The symmetry is such that an upward motion is dominating on the left-hand side of the roughness element and a downwash motion is dominating on the right-hand side. Furthermore, on the sides at z_c^* around -5 mm and around 35 mm, low-momentum fluid is lifted up from the surface, producing low-velocity streaks, and in the middle of the plot, behind the roughness element, an opposite motion is observed, where high-momentum fluid moves down to the wall forming the high-velocity streak in the boundary layer.

Because of the character of symmetry, namely the dominating upward motion to the left-hand side and the downwash motion to the right-hand side of the roughness element, a negative velocity streak is growing downstream to the left and the growth of a positive velocity streak is observed to the right (see figure 4). It can be noted also that the vortices are located rather far from the wall and the cores of the stationary perturbations lie outside the boundary layer. A superposition of the mean crossflow on the disturbance produces a motion as shown in figure 5(*c*) and the counter-rotating vortices are seen as a result. Here, we observe saddle-points at $z_c^* \approx -2$ mm, $y/\theta \approx 3$ and at $z_c^* \approx 37$ mm, $y/\theta \approx 5$. At the saddle-point $(-2, 3)$, periodic disturbances grow intensely, as shown in figure 5(*e*) and at point $(37, 5)$, secondary instabilities are triggered further downstream, as will be discussed later. The saddle-points are created
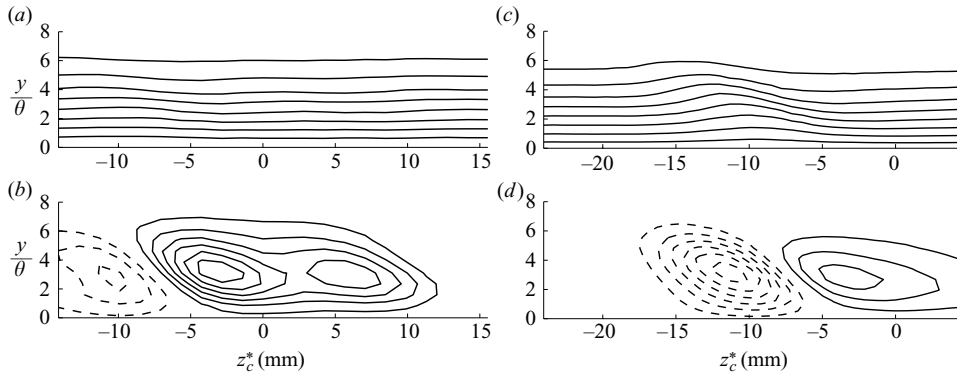
FIGURE 6. Contours of mean streamwise velocity and mean streamwise velocity disturbance at $x_c/c_c = 0.58$. (a, b) behind circular 8 mm diameter roughness element and (c, d) behind a hole with continuous suction. Contour levels used as in corresponding graphs of figure 5.

Case	Vortex generator	Roughness element size (mm)	$\Delta U_{0.5}/Q_0$ ($x_c/c_c = 0.58$)	$u^1_{max(y,z)}/Q_0$ ($x_c/c_c = 0.58$)
A	Left-hand side of roughness element	$35 \times 8 \times 0.39$	0.13	0.008
An	Left-hand side of roughness element	$35 \times 8 \times 0.39$	0.13	0.003 (natural)
B	Right-hand side of roughness element	$35 \times 8 \times 0.39$	0.09	0.015
Ar	Circular roughness element	$\oslash 8 \times 0.39$	0.04	0.004
As	Suction	–	0.12	0.014

TABLE 1. Different cases of excitation of crossflow vortex packets.

since the spanwise motion within the disturbance is opposite to the spanwise motion of the basic flow. From figure 4, we can also obtain an impression on the receptivity of the boundary layer to the long-wavelength (supercritical) excitation and it is seen that there is a limit of spanwise wavelength which can be excited, i.e. by increasing the length of the roughness element, the vortex scale will not increase further. Thus, even periodically distributed roughness elements of a large wavelength will most probably generate crossflow vortex packets.

Other cases studied are illustrated in figure 6, where the disturbance from a circular roughness element and the disturbance created by localized continuous suction are shown. As the spanwise roughness element size is shortened, the amplitude of the excited stationary disturbance in the boundary layer diminishes and the streak scales decrease. For a circular roughness element of 8 mm in diameter, the amplitude of the vortex at the station $x_c/c_c = 0.58$ reduces by about three times as compared to the 35 mm long roughness element. The wavelength of the generated vortices goes down to about 15 mm. Physically, the decrease of vortex magnitude can be explained by an interaction between the counter-rotating side vortices, which increases as the roughness element size is reduced. Localized continuous suction creates a vortex packet with dominating modes of about 20 mm in spanwise wavelength, i.e. of the same scale as the long roughness element. However, this method only allows the generation of a vortex packet of positive rotation similar to that generated by the left-hand side of the roughness element. The four cases focused on in what follows are summarized in table 1. As is shown, the roughness element height was 0.39 mm, which is nearly equal to the local momentum thickness. The quantity $\Delta U_{0.5}$ characterizes intensity
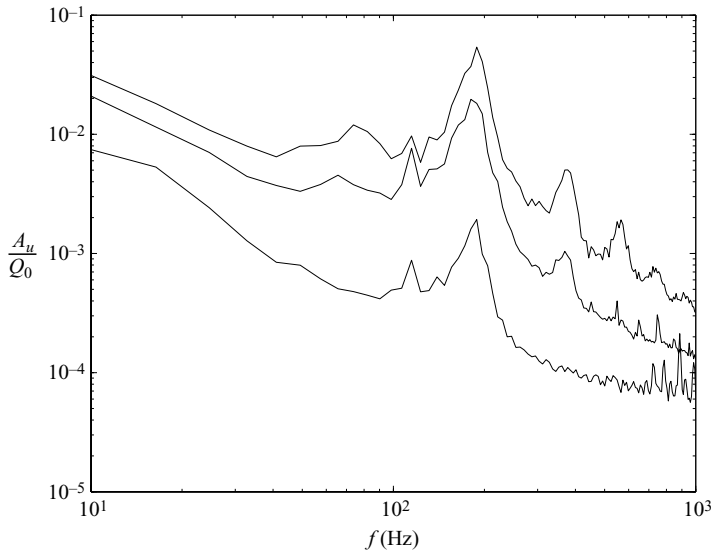
FIGURE 7. Amplitude spectra of natural secondary disturbance of the stationary vortex packet of Case A taken at streamwise stations $x_c/c_c = 0.55, 0.71, 0.77$ (from bottom to top) at positions of maximum disturbance r.m.s.

of the stationary disturbance, and $u^i_{max(y,z)}$ is the intensity of a time-periodic mode i, namely,

$$\Delta U_{0.5} = \tfrac{1}{2}\left(\max_{y,z}\{U'\} - \min_{y,z}\{U'\}\right), \tag{3.4}$$

$$u^i_{max(y,z)} = \max_{y,z}\{u'^i\}, \tag{3.5}$$

with U' being the stationary disturbance velocity and u' the time-periodic disturbance velocity. Two vortex packets generated by the 35 mm long roughness element which may have different stabilities are denoted as Case A and Case B. Case An differs from Case A only by way of secondary instability generation, which was not forced and appeared naturally in Case An. For the 8 mm diameter roughness element, the left-hand side vortex is dominating and the characteristics are given for this vortex, named Case Ar. In the fifth case, Case As, the stationary disturbance is generated by localized continuous suction through a hole of 0.8 mm in diameter with relatively high suction rate of the order of the local velocity Q_e. The localized suction (which is widely used for boundary-layer control purposes) acts on the flow almost in the same way as the surface roughness and, moreover, as was mentioned, rather high suction rates, i.e. energy is required so as to compare to the roughness-like actuator.

At first, secondary instabilities which occur naturally were studied and then, to allow phase-locked measurements, these disturbances were modelled and introduced artificially. In table 1, the amplitudes of the first harmonic of the periodic secondary disturbance, u^1, are given as measured at the station $x_c/c_c = 0.58$ with artificial periodic forcing (for all cases except Case An). The frequency of the disturbance was the same in each case, 210 Hz. This was chosen to be close to the frequency of the natural secondary disturbance as determined by the spectral analysis (see figure 7) where some data are shown for the natural secondary instabilities of the vortex packet in Case A. Here, the spectra are taken at the maximum of the secondary instability
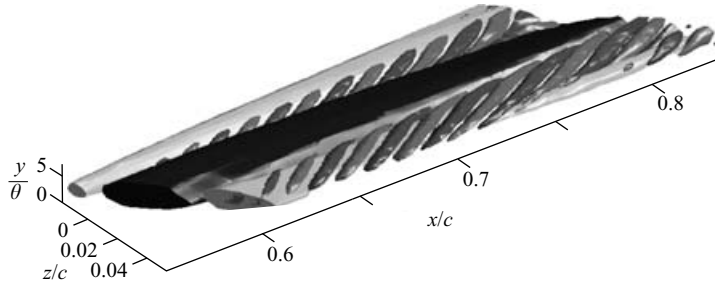
FIGURE 8. Forced periodical disturbances together with the stationary vortices of figure 4, Cases A + B are shown. Stationary disturbance isosurfaces are $\pm 6\%$ of Q_0, light isosurfaces of periodical disturbances: -0.5%, dark: $+0.5\%$ of Q_0.

within the cross-sections. The most amplified secondary perturbations are centred around 190 Hz, which is a dominating frequency in figure 7. The prevailing frequency is also the fastest growing one, indicating that the prevailing secondary instability mode is defined by the local growth rate at the onset point. What is remarkable is the appearance of higher harmonics of the instability as a periodical disturbance developing downstream. White & Saric (2005) hypothesize that the higher harmonics of the dominating frequency observed in their experiment could be independent secondary instability modes, rather than a result of nonlinear interaction. For the present experimental conditions, it was possible to give an answer to this question, which will be discussed later. It is necessary to note that under natural conditions, without artificial excitation, the secondary instabilities were developing and led to breakdown in all cases except Case Ar, which was stable in this sense. In what follows, the instability of these four configurations of the crossflow vortex packets is examined in a controlled manner and results of the natural instability of Case An are also provided.

An additional comment should be made on the procedure of the experiment in Case A and Case B. As depicted in figure 1 of the model set-up, only one blowing–suction hole is used for the secondary instability injection, and to trigger the instability the roughness element was moved in the spanwise direction for each configuration so that the stationary disturbance from one of the roughness element sides was developing over the blowing–suction hole. For a clearer demonstration the two experimental cases, A and B are superimposed in figure 8 in the same fashion as in figure 4. Figure 8 illustrates an important issue of the current experiment, namely that the two crossflow vortex mode packets, Case A and Case B, which are triggered by the long roughness element, are separated packets both in the sense of the stationary mean velocity disturbance and the unsteady secondary instability. Moreover, the current consideration of the vortex packets in the separate order is an important point of the transition modelling, since such packets (not symmetric and of different rotation) are most likely to be triggered under 'natural' conditions, as observed, for example, for a highly perturbed flow on the flat plate (see Brandt & Henningson 2002). During natural transition, as a rule, the secondary instabilities are also found to develop in localized fashion.

3.3. *Secondary instability of the crossflow vortex mode packets of Case A and Case As*

In this section, the crossflow vortex mode packets, Case A and Case As with the artificially triggered periodic disturbances, are in focus. The vortex of Case A is created by the left-hand side of the long roughness element and rotates clockwise,
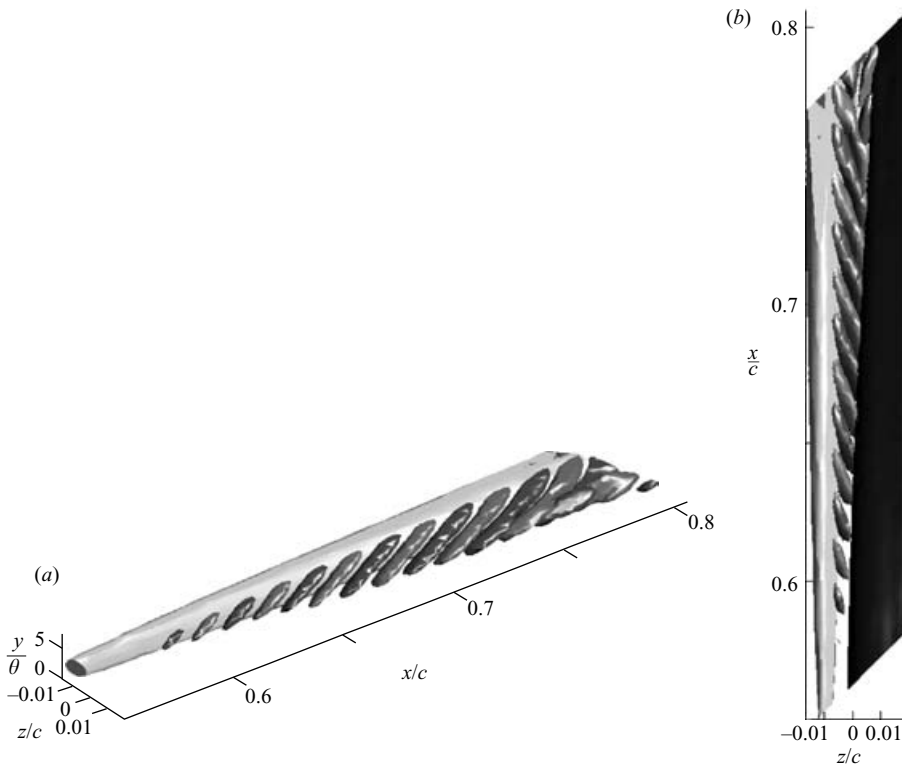
FIGURE 9. Mean and secondary disturbances of Case A are shown by streamwise velocity isosurfaces. Levels are as in figure 8. Note removed positive isosurface in (*a*).

against the base crossflow near the wall making the wake-type disturbance of the crossflow velocity component. First, an impression about the total disturbance field is given in figure 9, where the mean velocity distortion and the secondary perturbation are shown by isosurfaces of the streamwise velocity. In the figure, the x and z axes are shown in the same scaling to save proportions. Zero of the spanwise axis coincides with the location of the periodic point source and the streamwise coordinates are given as the distance from the airfoil leading edge on the line of $z = 0$. This figure is a single frame of obtained time-dependent hot-wire visualization and to clarify the spatial structure of the secondary disturbance the visualization is shown in figure 9 from two different viewpoints. The stationary disturbance develops approximately along the x-axis, hence the wind-tunnel-fixed coordinate system nearly coincides with the vortex-oriented coordinate system and the same is also true for the external-streamline coordinate system because the external flow angle is nearly 44°.

From this graph, considering the development of the stationary disturbance, it can be noted that for this stationary vortex packet, the low-speed streak is growing downstream, while the high-speed streak is virtually unchanged. This is probably extending from the dominating upward motion of the stationary disturbance as compared to the downwash motion (recall figure 5*d*). The secondary instability disturbance, as can be deduced from the visualization of figure 9, is developing in the area of strongest spanwise gradient of the streamwise velocity, between two stationary streaks. What is remarkable is a spatial localization of the disturbance. A description of the periodical disturbance is complicated by an extremely three-dimensional
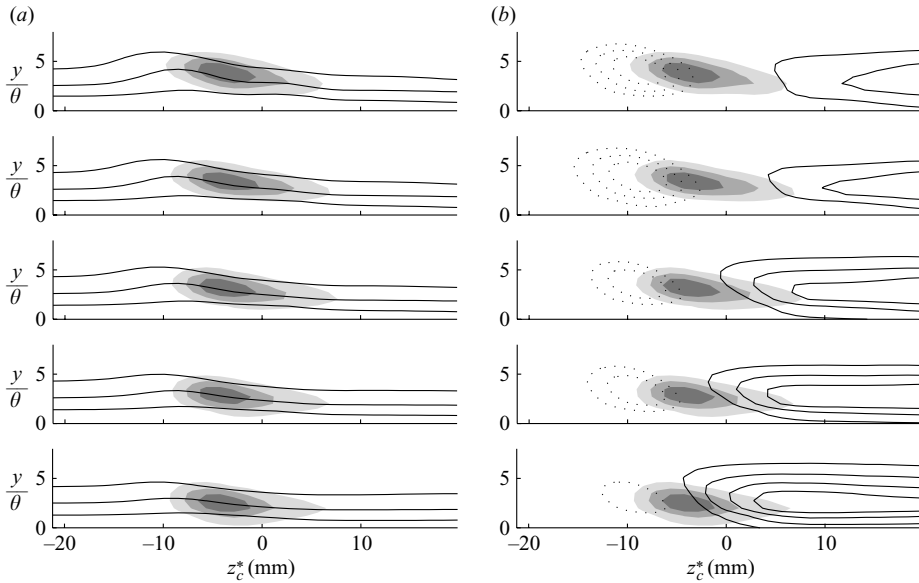
FIGURE 10. Contours of (*a*) mean streamwise velocity, U and (*b*) mean streamwise velocity disturbance, U' with imposed first harmonic of secondary disturbance, u^1 (shading), Case A. $x_c/c_c = 0.56, 0.61, 0.65, 0.70, 0.74$ increasing from bottom to top. Contour levels for U are 25, 50, 75 % of U_e; for U' the contour step is 25 % of $\Delta U_{0.5}$ and nearest to zero contour levels not shown; for u^1 levels are 25, 50, 75 % of local maximum. Negative values of contours are shown by dotted lines.

character of the secondary instability, so that the commonly used representation in the frame of amplitudes and phases is too cumbersome and the present volumetric graph seems to be the most effective one.

The correlation between the stationary vortex and the secondary instability is shown in more detail in figure 10. In this figure, contours of mean streamwise velocity as well as of mean streamwise velocity disturbance are shown with imposed secondary disturbance for several streamwise positions. The periodical perturbation is introduced at $z_c^* = 0$, while the induced disturbance appears about 4 mm to the left. For the current case, saturation of the stationary disturbance happens only far downstream, near the last section shown in the figure. This can also be deduced from the shape of the deformation of the mean flow contours, since this is a good indicator of the vortex state. In particular, a comparison can be made with the illustrations given in the works by Wassermann & Kloker (2002) and White & Saric (2005). As it is possible to see from figure 10, the stationary vortex is amplified significantly during the downstream development and the same is true for the secondary disturbance. The fact that the appearance of the secondary instability is possible prior to the saturation of the crossflow vortex is in accordance with some previous works (Boiko *et al.* 1997; Malik *et al.* 1999), however, this phenomenon was not emphasized before. From figure 10, we can immediately deduce that the secondary disturbance develops in the area of highest spanwise shear, which is very typical for the 'z' mode of the secondary instability. At the beginning of the vortex development, two areas of high spanwise shear exist and the minimum of $\partial U/\partial z$ is located approximately at $z_c^* = -13$ mm, while the maximum is approximately at $z_c^* = -4$ mm. A second maximum appears later on, after $x_c/c_c = 0.65$ at $z_c^* \approx 4$ mm.

The secondary disturbance, hence, is correlated well with the location of the positive extremum of the spanwise gradient of streamwise velocity. Also at this location, the perturbation of spanwise velocity has its negative extremum and the secondary disturbance lies within the wake part of the W-velocity component. In Wassermann & Kloker (2002), the secondary 'z' mode was found to be situated at the position of maximum negative spanwise gradient, i.e. in a gradient of opposite sign; however, in our case, the crossflow component of the base flow also has the opposite direction to that in the study of Wassermann & Kloker (2002). In the position of maximal negative W-disturbance, where the instability is located, the gradient $\partial W/\partial z$ is zero. The strongest upwelling motion is located within the low-speed streak. It should be noted that the three-dimensional nature of the flow on the swept wing makes identification of the factors for the secondary instability onset more complicated, as compared to two-dimensional flows and both U and W velocity components should be taken into account. Indeed, the secondary disturbance has very high obliqueness as is shown in figure 9 and the wave vector of the disturbance is almost parallel to the wing leading edge, while the disturbance is developed nearly along the x-axis. For such a wave, both components of mean velocity are of significance.

Some workers (Koch *et al.* 2000) particularly note an important role of the spanwise velocity component and its gradient, while correlations by Wassermann & Kloker (2002) are based purely on the consideration of the streamwise component. In principle, these two attitudes are complementary, since components of the velocity vector are bounded by the Navier–Stokes equations; however, in the present case the $\partial U/\partial z$ gradient seems to play a dominating role. At the same time, for the vortex packet and the secondary disturbance as in those in Case A, experiments by Litvinenko *et al.* (2003) demonstrate that by reducing the spanwise shear of the streamwise velocity, it is not always possible to affect the secondary perturbation, thus the crossflow motion must be taken into account. Furthermore, from figure 10, it is clear that the artificial disturbance is located in the same area as the natural secondary disturbance of figure 5(*e*). As was mentioned in §3.2, the location of the secondary instability correlates with a saddle-point of crossflow velocity components, which is an additional criterion for identification of the secondary instability onset. Points of this type may be evaluated in experiments/calculations as having a magnitude of stationary spanwise perturbation velocity extremal and opposite to the local base flow spanwise velocity. As can be seen in figure 10, both the primary and secondary disturbances are weakly dispersive and the conservation of the spatial amplitude function of the secondary perturbation suggests that this mode is an eigen-mode of the three-dimensional distorted flow. To our knowledge, this fact was never observed and confirmed experimentally.

As the secondary disturbance evolves downstream, it affects mean velocity and becomes distorted, which implies that nonlinear interactions between the stationary and the travelling modes become significant. An indication of this process is the appearance of higher harmonics of the main frequency of the travelling disturbance. First and second harmonics of the travelling disturbance are shown in figure 11. As is obvious, the maximum of the second harmonic is highly correlated with that of the first harmonic. An early conclusion which can be drawn from the above data is that the second harmonic is a product of the nonlinear interactions rather than of an additional travelling mode. Figure 11(*a*) also shows that the secondary disturbance is highly correlated with the critical layer, where local velocity is equal to the phase velocity of the disturbance. An interpretation of this fact is that the
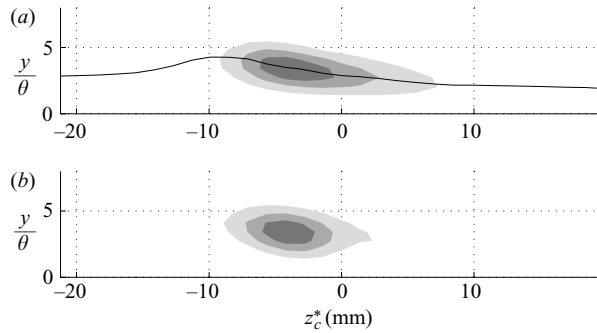
FIGURE 11. (*a*) First and (*b*) second harmonics of the secondary disturbance at $x_c/c_c = 0.69$ shown for Case A. Solid line denotes critical layer, shading indicates 25, 50 and 75 % levels of the local maximum of perturbations.

secondary instability travels with the local flow velocities and this is very typical for instabilities of the inviscid type.

The crossflow vortex mode packet in Case As differs from that in Case A by the method of the disturbance generation and in Case As the continuous localized suction was used. A generated stationary vortex packet differs somewhat from the packet of Case A (cf. figures 6*c*, *d* and 5). In particular, the spanwise scale of the positive streak is much smaller in Case As. However, since the amplitudes of the vortex packets in cases A and As were very close and amplitudes of the secondary travelling disturbance were comparable, the spatial structure of the secondary disturbance in Case As was not significantly different from that in Case A. Higher amplitude of the secondary disturbance led to earlier nonlinear interactions, in particular, superharmonics were generated faster.

In the following sections, secondary instability of other crossflow vortex mode packets is considered and, as will be demonstrated, the secondary stability properties of such packets are altered.

3.4. *Secondary instability of the crossflow vortex mode packet of Case B*

In Case B, the stationary vortex is created by the right-hand side of the long roughness element; this spanwise-localized vortex rotates counterclockwise, co-flowing the base crossflow near the wall and the disturbance of the crossflow velocity component is of jet-type. Receptivity of this vortex packet with respect to the secondary disturbance was found to be lower as compared to Case A, so that the amplitude of the periodical blowing-suction was increased to about twice that in Case A. The total disturbance field is given in figure 12, where again the mean velocity distortion and the secondary perturbation are shown. In this figure, the zero of the spanwise axis also coincides with the location of the periodic point source, and the streamwise coordinates are given as a distance from the airfoil leading edge on the line of $z = 0$. As is seen, the stationary disturbance has nearly the same obliqueness angle as in Case A, however, the low-speed streak is more spread out, thus stationary modes grow in a different way as compared to Case A, indicating that the nonlinear effects are of importance for the development of the stationary disturbance. Additionally, it can be noted that for this stationary vortex packet the high-speed streak is growing downstream and the amplitude of the low-speed streak is nearly conserved. Hence, the stationary disturbance behaves virtually in an opposite fashion as compared to Case A, where the low-velocity streak was amplified. Again the explanation lies in the formation
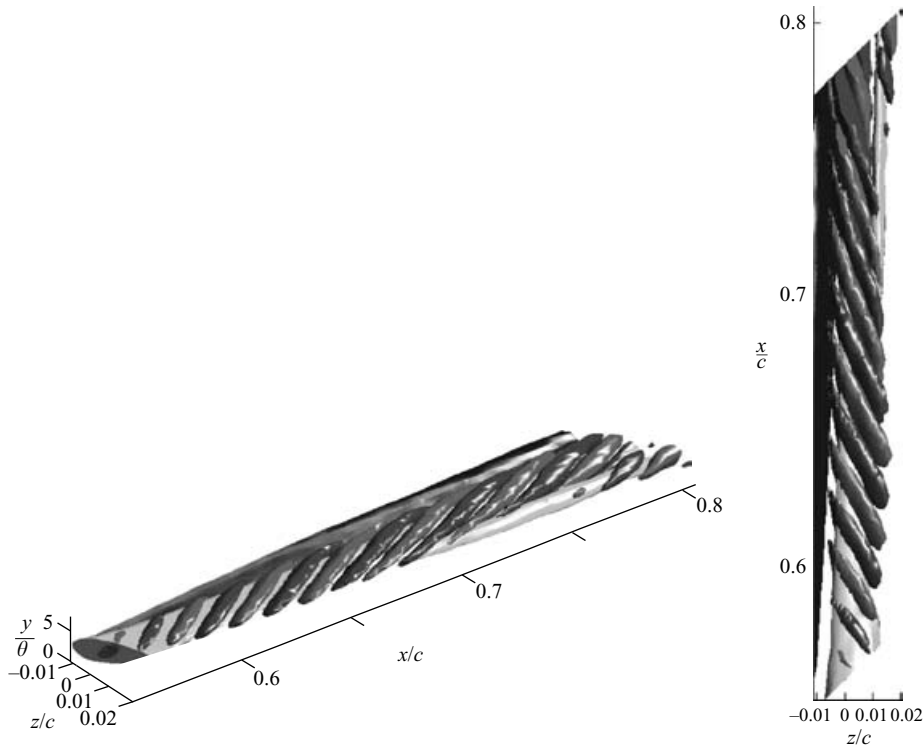
FIGURE 12. Mean velocity distortion and secondary disturbance of Case B shown by streamwise velocity isosurfaces, the values for isosurfaces are as in figures 8 and 9.

of disturbance (cf. figure 5d), since the downwash motion is dominating over the upward motion. Another, and more important difference, as compared to Case A, is the location of the secondary instability disturbance, which is developing inside of the low-speed stationary streak. The secondary disturbance is space-localized as well and it seems that the spanwise extent of the secondary instability is dictated by the spanwise scale of the stationary low-speed streak. From the graph, we can also see that the angle of the phase velocity vector of the periodical disturbance increases with streamwise distance. It is possible to explain this effect by nonlinear interaction of the travelling disturbance with the mean flow. Such a clear change of the obliqueness of the travelling-wave packet is not visible for the secondary disturbance considered previously, in Case A.

Details of the stationary vortex and the secondary instability development are shown in figure 13. As can be seen, the stationary disturbance, as for Case A, saturates near the last section and the discussions of § 3.3 are also appropriate to Case B. Also, a secondary disturbance shift from $z_c^* = 0$, where it was introduced, can be observed, however, the shift now is nearly 4 mm to the right. Again, the induced secondary disturbance seems to be located in the most favourable position. Furthermore, a significantly larger dispersion of the low-speed streak can be observed as compared to the streak of the vortex packet Case A. The secondary perturbation reveals conservation of the shape of the amplitude function at the initial stage of its development, and nonlinear effects cause subsequent change of the amplitude function. At the early stage, it is most likely that the eigen-mode is triggered in the flow. Figure 13 clearly demonstrates that the secondary perturbation develops within
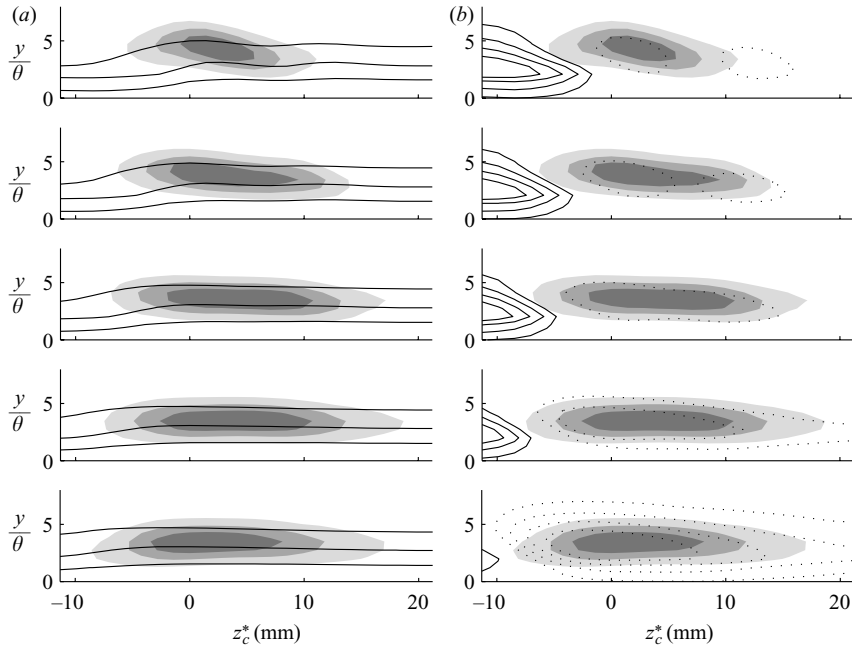
FIGURE 13. Contours of (*a*) mean streamwise velocity and (*b*) mean streamwise velocity disturbance with imposed first harmonic of secondary disturbance (shading) for Case B. Streamwise coordinates and levels are as in figure 10.

the low-speed streak, where the spanwise gradient of the streamwise velocity is nearly zero, hence, the mode of the secondary instability differs from the 'z' mode.

The secondary disturbance is spanning the whole streak width and, in addition, we can see that this perturbation is located somewhat further from the wall as compared to Case A. Also, the maximum of the secondary disturbance is slightly off the low-speed streak minimum. As has been pointed out by Malik *et al.* (1999), the secondary instability modes on the swept wing can be classified by the energy production associated with either the surface-normal or the spanwise gradients as 'y' or 'z' modes. Performing analysis of the U and W velocity profiles, it was found that the location of the secondary instability correlates with the minimum of the wall-normal gradient of spanwise velocity. Both $\partial U/\partial z$ and $\partial W/\partial z$ gradients do not reveal extrema at this location. Furthermore, a comparison with Wassermann & Kloker (2002) can be made, where the 'y' mode is also located within a low-speed streak in the region of strong upwelling fluid motion. Hence, the character of the disturbance testifies to a 'y' mode of the crossflow secondary instability. In principle, this is consistent with an observation of Bottaro & Klingmann (1996) for the instability of Görtler vortices, namely that sinusoidal modes of instability prevail in vortices with small spanwise wavelength while varicose modes dominate long-wave vortex structures. Asai *et al.* (2002) for streaks in Blasius flow also deduced that when the low-speed streak is wide it becomes more unstable to the symmetric modes than to the antisymmetric modes. Physically, it is probably because the vortices with large wavelengths provide weaker spanwise shear and the vortices with short wavelengths induce a strong one. This, particularly, is true for a magnitude of positive $\partial U/\partial z$ gradient, which is significantly weaker in the current experimental Case B as compared to Case A. Also note that while the secondary instability disturbance of Case B is located near the point of
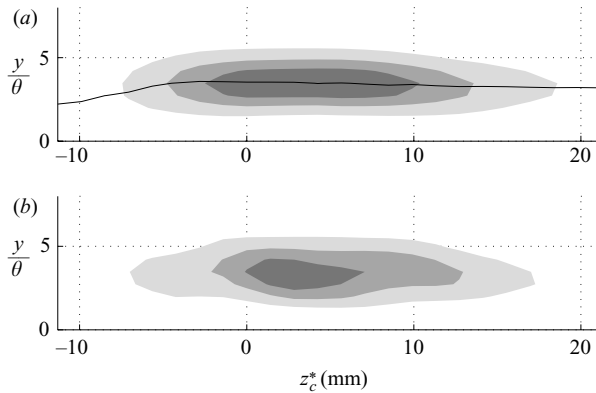
FIGURE 14. (*a*) First and (*b*) second harmonics of the secondary disturbance at $x_c/c_c = 0.60$ shown for Case B. Solid line denotes critical layer, the levels of perturbations are given as in figure 11.

inflection of the spanwise velocity, the perturbation of this velocity component by the stationary vortex packet is rather small (see figure 5*c*), and the presence of the low-speed streak seems to be of importance for the secondary instability onset and development.

As a travelling disturbance develops downstream, its amplitude increases and nonlinear interactions become significant. In the current Case B, similarly as in Case A, flow breakdown occurs with the generation of higher harmonics of the main disturbance frequency. The location of the second harmonic with respect to the first is shown in figure 14. As for Case A, the first and second harmonics of the travelling disturbance are very well correlated, as can be seen in this figure. The critical layer is depicted in figure 11(*a*) and it is observed that this mode of secondary instability also travels with the local flow velocities.

3.5. *Influence of the primary vortex packet amplitude on the secondary instability development (Case Ar)*

As was found, breakdown of the stationary vortex packet owing to the development of a secondary periodical disturbance occurs when the amplitude of the primary stationary perturbation exceeds a certain critical value. At the same time, it is not a mandatory condition for the stationary vortex to saturate. Existence of a threshold for the secondary instability is noticed by most workers and to verify the threshold conditions, a crossflow vortex packet of lower amplitude was generated in the swept-wing boundary layer. A decrease of vortex amplitude was obtained by reducing the spanwise extent of the vortex generator (roughness element). The roughness element used had cylindrical shape and this case is called Case Ar. As was discussed earlier, in this case, the crossflow vortex packet is formed with the interacting side vortices produced by the spanwise edges of the roughness element. As a result, the amplitude of the stationary disturbance was reduced to about three times that in Case A. Subsequently, the vortex packet development did not lead to laminar-flow breakdown and growing secondary instabilities did not appear. To excite the travelling disturbance, the amplitude of the periodic blowing–suction was increased to about four times that in Case A.

The circular roughness element initiates a crossflow vortex packet producing streaks, as shown in figure 15(*a*). Two streaks are visible here and the third one of low speed
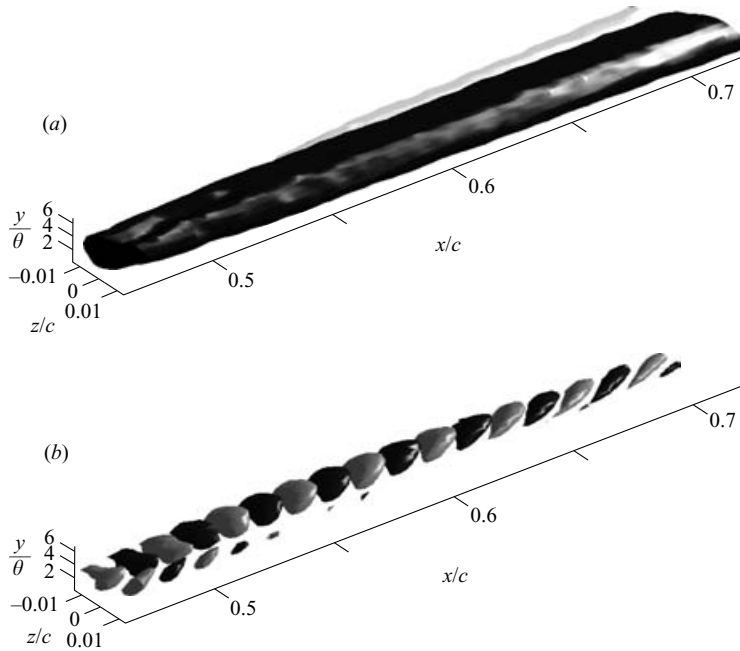
FIGURE 15. (*a*) Mean velocity distortion and (*b*) secondary disturbance of the vortex packet in Case Ar shown by streamwise velocity isosurfaces. Those of the mean disturbance are $\pm 1.2\%$ of Q_0 and those of the periodical disturbance are $\pm 0.1\%$ of Q_0.

exists to the right-hand side of the roughness element, however, it has a very low amplitude and is not seen at the given level of isosurfaces. In figure 15(*b*), the triggered periodical disturbance is presented. A close consideration of the travelling perturbation suggests that the excited wave packet is somewhat different from the wave packet in Case A. In particular, initially a large portion of the secondary perturbation is located within the low-speed streak and this part of the wave packet is diminishing in amplitude while travelling downstream. After a streamwise coordinate of 0.65 chord, the shape of the wave packet and its location is becoming closer to those of the 'z' mode in Case A. Furthermore, the amplitude of the wave packet is nearly constant at different streamwise stations.

A contour slicing of several streamwise positions shows the stationary and the periodical disturbances in detail (see figure 16). As can be seen, the contours of total mean velocity are only slightly deflected, even at the most downstream section. Notably, in spite of the obvious nonlinearity of all vortex packets studied, the two parts of the stationary vortex packet in Case Ar are like those in Case A and Case B. The process of formation and evolution of the vortices is very similar, namely, the left-hand side of the narrow width roughness element generates a vortex as in Case A and on the right-hand side, the vortex is as in Case B. Also, substantial growth of the low-speed streak is observed to the left and the high-speed streak increases in amplitude with the streamwise development to the right of the roughness element. Thus, despite the nonlinearity of the vortex packets, their formation and development is governed by simple physical mechanisms.

Considering the periodical disturbance, it can be noted that its projection on the (y, z)-plane is similar to the secondary disturbance in Case A and does not reveal its different three-dimensional aspect as the volumetric visualization does. The periodical
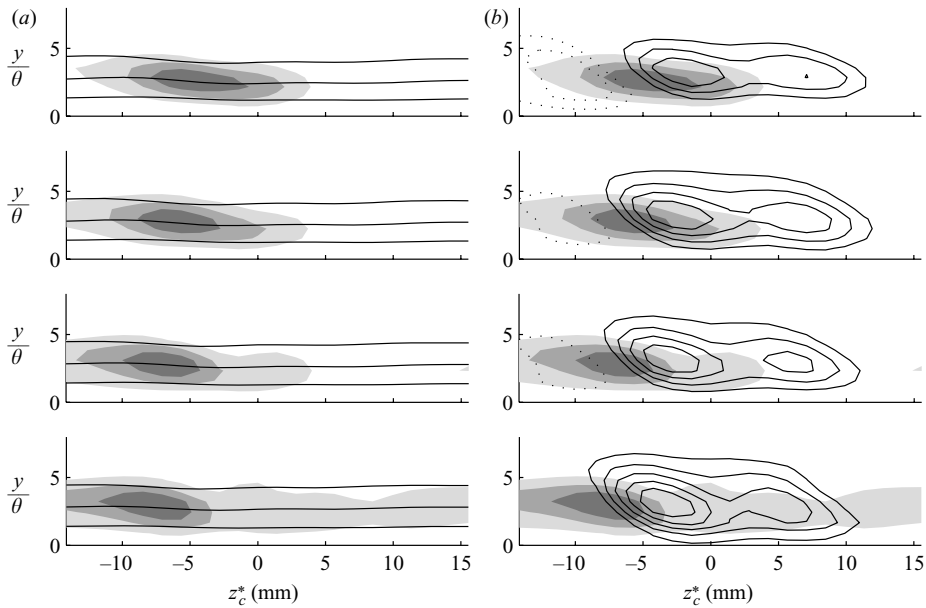
FIGURE 16. Contours of (*a*) mean streamwise velocity and (*b*) mean streamwise velocity disturbance with imposed first harmonic of secondary disturbance (shading), Case Ar. $x_c/c_c = 0.54$, 0.58, 0.63, 0.67 from bottom to top. Contour levels are as in figure 10.

disturbance generated in the flow, despite the rather high amplitude of forcing, is of significantly lower amplitude as compared to Case A and, as the contour shading demonstrates, the amplitude of the travelling disturbance is virtually unchanged while the perturbation is developing in the streamwise direction. Also as seen, the excited periodical disturbance has completely died out around the spanwise coordinate of the excitation, $z_c^* = 0$ and exists far to the left. A further note is that the stationary vortex packet with the travelling instability is visibly convected to the right in figure 16, while developing downstream, which was not observed in the previous vortex packet cases. It seems that this lower-amplitude vortex lies deeper in the boundary layer and does not extend much outside, thus it is more affected by the base crossflow near the wall.

3.6. *Further considerations*

In the previous sections, different stationary crossflow vortex mode packets and their secondary instabilities were considered. It is demonstrated that triggered secondary instabilities depend mainly upon the character of the primary stationary vortex and are of inviscid character. In this section, the mechanisms driving the secondary instabilities are considered in more detail.

The summary of the two instability modes investigated is presented in figure 17. It is obvious that the formation of the localized areas of non-uniform flow (streaks) cause the non-equilibrium flow and, in order to return to uniformity, the flow tends to smooth out these areas. Such processes are also very common in different generic flows. Considering figure 17, we can associate breakdown of a low-speed streak in the swept-wing boundary layer via the '*z*' instability mode with the breakdown of a plane shear layer. The breakdown of a low-speed streak via the '*y*' instability mode can be related to the breakdown of the wake behind a bluff body. However, in the swept-wing
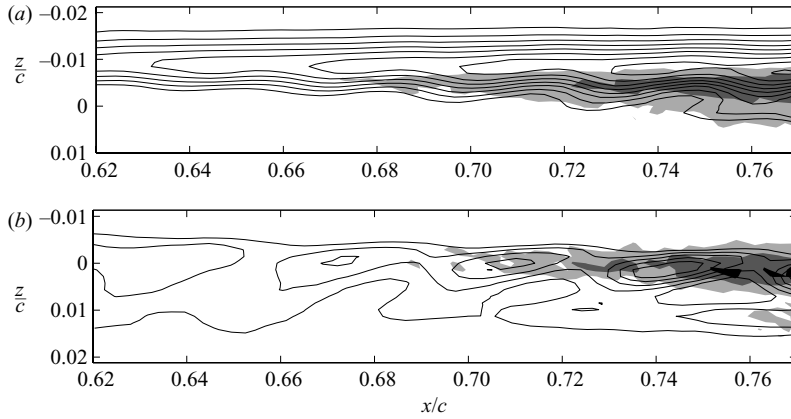
FIGURE 17. Contours of total streamwise velocity disturbance (mean and periodic part) with r.m.s. shading. Negative isolines are shown. The development of (*a*) '*z*' and (*b*) '*y*' modes of secondary instability is depicted.
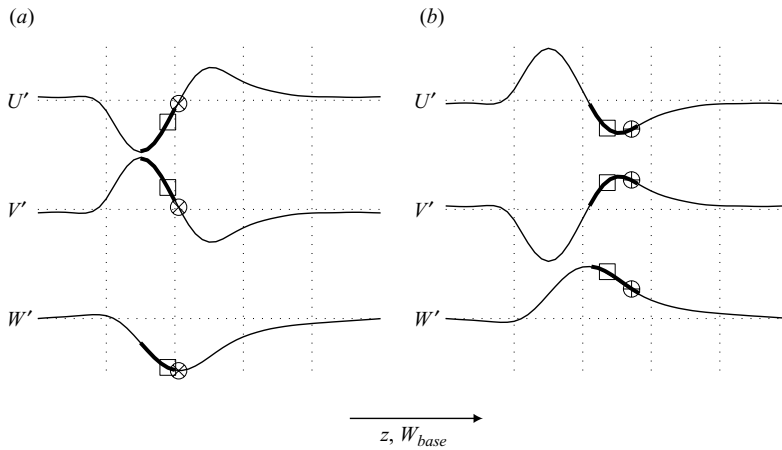

FIGURE 18. Schematic of disturbance velocity distributions of two basic crossflow vortex mode packets. (*a*) Localized vortex of positive rotation with preferred '*z*' mode of secondary instability and (*b*) Localized vortex of negative rotation with preferred '*y*' mode of secondary instability. Symbols mark observed location of maxima of secondary instability. Natural instability: ×, high-frequency and □, low-frequency instability in the present experiment; +, broadband fluctuations in experiment of Boiko *et al.* (2000). Forced secondary instability: ○, present experiment; bold lines, experiment of Kozlov *et al.* (2001).

boundary layer the flow symmetry is changed owing to crossflow and the symmetry of the breakdown is apparently different. Also, as was demonstrated, the developing disturbances are of obvious three-dimensional character. It is well known that the characteristics of secondary instability in boundary layers are strongly dependent on the primary instability affecting the secondary disturbance frequencies, amplification rates, origination and dominance of a distinct type of instability and these factors are coupled by complex equations.

To distinguish the two modes of secondary instability more carefully, a schematic diagram is represented in figure 18. As was observed, the major difference between

the two primary vortex packets investigated is created because of the different signs of their rotations (or sign of the streamwise vorticity component, ω_x) and this is reflected in the diagram. The vortex packet in figure 18(*a*) has positive streamwise vorticity, the vortex packet shown in figure 18(*b*) has negative streamwise vorticity and the direction of the base crossflow is assumed to be positive. A localized vortex with positive rotation has mean velocity distributions as depicted in figure 18(*a*) and the localized vortex having negative sign of rotation (counterclockwise) as in figure 18(*b*). In the scheme it is assumed that these two vortex packets have all three perturbation velocity components of the opposite sign. In spectral space, this appears as a shift of all the streamwise stationary modes by π radians in phase. It is clear that from the viewpoint of the secondary instability theory (see e.g. derived equations by Malik *et al.* 1994), these two vortex configurations would create different conditions for the secondary perturbations since some of the production terms in the equations are not the same. In particular, the sign of strongest gradient $\partial U/\partial z$, the modification of crossflow velocity, which either increases or decreases the existing crossflow and the width of the formed low-speed streak are different.

Considering our experiment, we can correlate the vortex packet model in figure 18(*a*) with the stationary vortex packet in Case A and the model in figure 18(*b*) with the stationary vortex packet in Case B, respectively. In fact, the diagrams are drawn based upon the experiment. The observed location of the maxima of secondary instabilities with respect to the vortex packets is marked on the diagrams as was seen during the tests. The summary is made from the present results and from results of Boiko *et al.* (2000) and Kozlov *et al.* (2001). In the present experiments, natural low-frequency (around 25 Hz) secondary instability packets were observed and in the previously discussed figure 5(*e*), the broadband disturbance located at $z_c^* = 30$ mm consists primarily of this frequency. In Case A, the low-frequency instability is located slightly off the high-frequency mode, just on the side of the low-speed region and in Case B, this instability is closer to the area of the highest spanwise shear, being within the low-speed streak. It is seen that for both positively and negatively rotating vortices, the secondary disturbances are located either inside the area of streamwise velocity deceleration or near the position of highest spanwise gradient of this velocity component. As our analysis revealed, the preferred secondary instability modes of the vortex packet with positive rotation are of '*z*' type and the preferred modes of the vortex packet with negative rotation are of '*y*' type. As can be seen, the presence of a strong positive $\partial U/\partial z$ gradient (of the same sign as the base crossflow) favours the '*z*' mode of secondary instability. As this gradient is weak and the low-speed streak is wide, the instability mode of '*y*' type is established within the low-speed streak.

Experimental velocity profiles behind the 35 mm roughness element are shown in figure 19. Spanwise profiles of streamwise velocity are given in figure 19(*a*) and a clear relation can be found with the previously discussed figure 18. Also, it can be seen why the vortex packets are more unstable as compared to single-mode disturbances. Within the vortex packet, possible velocity distortions are significantly sharper than in sinusoidal-like stationary vortices and in this sense the vortex packet is similar to the saturated single-mode vortex, although the individual spectral components of the packet are not yet saturated. The simplified explanation would be as follows. The maximum gradient due to a sinusoidal disturbance of amplitude A having wavenumber α_z is $\alpha_z A_{max}$ and for the packet of modes, the largest possible gradient would be a sum of the gradients due to each mode $\alpha_{z1} A_{max1} + \alpha_{z2} A_{max2} + \cdots$ and so on, thus higher. Then, the observed spanwise profiles are closer to a tangent hyperbolic shape than to the shape of a sinusoid.
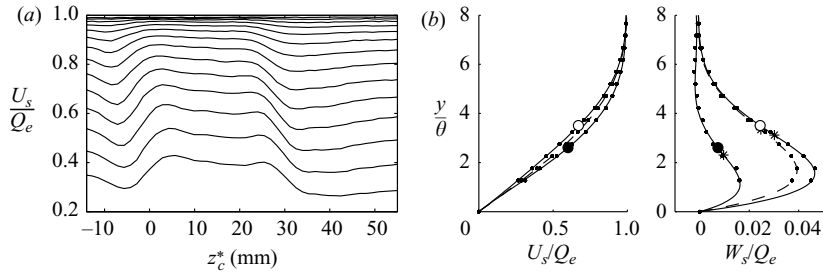
FIGURE 19. Experimental velocity profiles at $x_c/c_c = 0.54$ behind 35 mm roughness element. Data in (*a*) corresponds to $y/\theta = 1.28, 1.77, \ldots, 7.66$. Measured values in (*b*) are denoted by dots, lines are polynomial data fit, dashes denote undisturbed profiles, stars mark the inflection of the fitting polynomials. ○, observed wall-normal location of '*y*' mode of secondary instability at $z_c^* = 40$ mm; ●, wall-normal location of '*z*' mode of secondary instability at $z_c^* = -3$ mm.

At the same time, the wall-normal velocity profiles in the present case are not significantly distorted, as shown in figure 19(*b*). In this figure, inflection points and the location of secondary disturbances are also marked. In the present case, the substantial modification of the crossflow velocity component (either promotion or reduction) by the primary vortex, as shown in figure 19(*b*), mainly affects the location of the secondary instability with respect to the wall, which is strongly correlated with the inflection point of the crossflow velocity component. This is true for both '*y*' and '*z*' secondary instability modes. At the same time, the correlation with the inflection of streamwise velocity is not observed. It seems that the most amplified secondary instability modes in the study of Wassermann & Kloker (2002) are as well correlated with the inflection point of the crossflow velocity component. Thus, we can see a relationship between the primary instability of a flow and the secondary instability of the same flow modified by a large-amplitude disturbance so that the driving mechanisms seem alike. This idea can also be supported from another viewpoint. If we consider the secondary instability of the streaks in different flows, we will see that there is an apparent relationship between the critical Reynolds number of the flow and the critical amplitude of the streaks. For example, in a plane Poiseuille flow, reported values of the critical streak amplitude, which is necessary for the secondary instability onset, $\Delta U_{0.5}$, are around 35 % (Elofsson *et al.* 1999), in a Blasius boundary layer they are close to 25 % and 40 % (Andersson *et al.* 2001; Asai *et al.* 2002), respectively, for sinuous and varicose secondary instability modes, and in a two-dimensional flow with adverse pressure gradient they are about 15 % (Kozlov *et al.* 2004).

For a given flow, the threshold value seems not to be affected by a change of Reynolds number because of the inviscid character of the secondary instability. The presence of the crossflow velocity component significantly decreases the stability of the swept-wing flow besides the effect of the adverse pressure gradient. Since the critical Reynolds number is lower, it seems that the threshold for the secondary instability onset, as compared, for example, to the Blasius flow or the swept wing flow with favourable pressure gradient, would decrease.

Streamwise development of the stationary primary disturbances and of the secondary instabilities is shown in figure 20. The magnitude of $\Delta U_{0.5}$ was identified along the spanwise extent, as was shown in the previous visualization figures for the corresponding cases. The saturation of the two strongest vortex packets can be observed after a streamwise coordinate of about 0.7. The similarity of the growth of the vortex packets in Case A and Case B seems to be because these vortices are
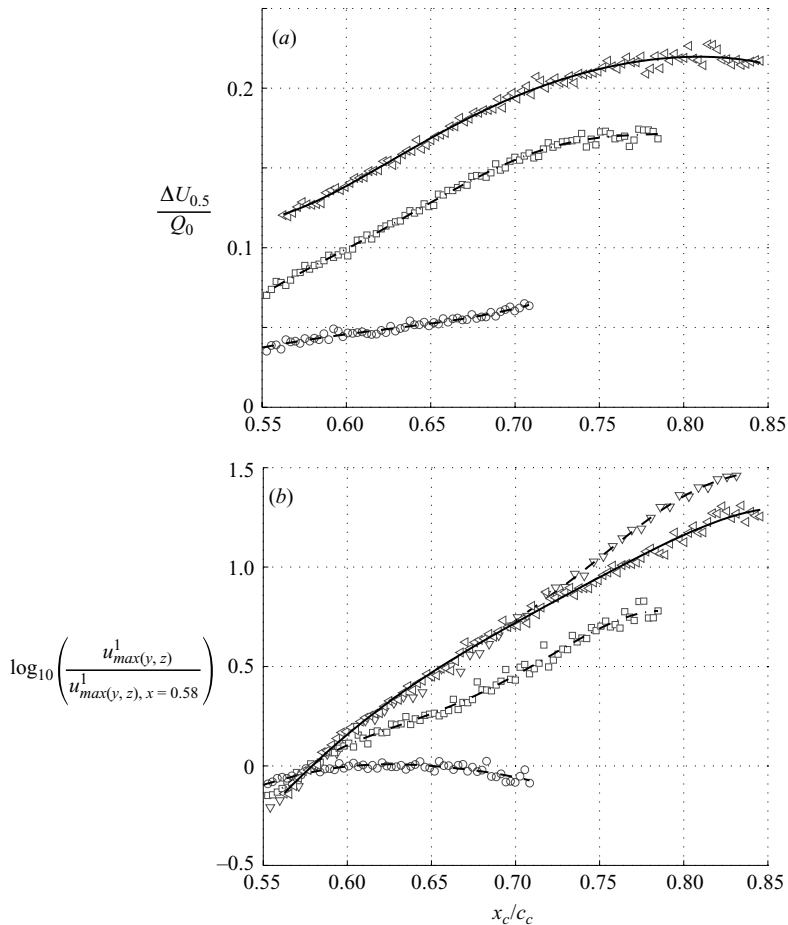
FIGURE 20. Downstream development of (*a*) the stationary disturbance and (*b*) first harmonic of high-frequency secondary instability for different cases studied. Symbols are from experiment and lines are polynomial data fit. ◁, Case A; □, Case B; ○, Case Ar; ▽, Case An. Amplitude of the first harmonic of secondary disturbance at $x_c/c_c = 0.58$ is given in table 1.

generated by two different sides of the roughness element and might really have the same streamwise vorticity but of different sign. In turn, the modal decomposition of these disturbances is not so straightforward to interpret and demonstrate strongly nonlinear behaviour of the separate spanwise modes. As was discussed previously, the secondary instability onset is mostly associated with the spanwise gradient of streamwise velocity and with the presence of local areas of low-momentum fluid (low-speed streaks). The criterion of $\Delta U_{0.5}$ seems to reflect adequately both these factors and so far is conventionally used for the prediction of secondary instability in different flows. From the point of view of an experimentalist, it is also important that its value can be identified in the experiment with relative ease and good accuracy. In the current case it was found that the threshold value of $\Delta U_{0.5}$ for the secondary instability onset is approximately 7–10 %.

If a comparison of the growth of the natural secondary instability and the growth of the artificially excited mode within the vortex packet in Case A is made, it will be seen that down to the section x_c/c_c of about 0.7, the growth is independent

of the initial disturbance amplitude and this happens despite the amplitudes of secondary instabilities reaching significant values prior to this position (about 4 % in Case A and 2 % in Case An). The independence of the growth from the initial amplitude indicates a linear behaviour of the secondary instability. The linearity of the travelling disturbances, such as that in Case A, was testified in more detail in Boiko *et al.* (1997). In addition to the linearity of the perturbations at the initial stage, they proved independence of the disturbance propagation velocity along the vortex from the amplitude, the way of excitation and frequency. Also, they demonstrated the fulfilment of the superposition principle for the waves by showing that interaction of waves of different frequencies (combinational modes) did not appear up to their total amplitude of about 1 %.

The linear behaviour of the waves indicates that they represent a secondary linear instability of the flow, being therefore a subject for secondary instability theory. At the same time, it is not necessary for these waves to be eigenmodes, i.e. with amplitude eigenfunctions. Usually, a certain distance is required for the disturbance to convert to the eigenmode and, as a result, the eigenmode theory would not necessary precisely predict the growth of the waves from their very origin. Furthermore, from figure 20 it is possible to observe that initially the growth rate of the 'y' mode of secondary instability (Case B) is several times lower that that of the 'z' mode (Case A and Case An), while nonlinear growth of these two different modes after $x_c/c_c = 0.65-0.7$ is nearly the same. In the subcritical Case Ar, the secondary instability disturbance is nearly neutrally stable since its amplitude is almost constant. It is necessary to note that to obtain the values of u^1, which are shown in this graph, maximum amplitudes of the disturbance were determined from the velocity maps, see (3.5) for definition.

The character of the development of the superharmonics of secondary instabilities (figure 21) suggests their nonlinear origin from the main harmonics. We can see that the total amplification of the second harmonic over the x-range shown in the figure in both cases is (about twice) higher than that of the main mode, while the third harmonic grows even faster (about triple). Such behaviour is very typical for the nonlinearly generated disturbances. Hence, it is possible to conclude that these modes are produced nonlinearly from the main secondary instability modes.

Since the growth of the 'z' and 'y' modes of secondary instability is different, it is important to know the conditions which favour one or the other instability mode. Then it might be possible to control the flow in the sense of avoiding, for example, onset of 'z' modes. Of course, one possible way of flow control immediately arises from the consideration of the vortex packet created owing to the circular roughness element in Case Ar, since, firstly, it was shown that the interaction of the counter-rotating vortices on the sides of the roughness element leads to the mutual damping of the vortices and secondly, that the flow excitation at subcritical wavelengths produces lower growth of the vortices. The latter effect is very similar to the idea behind the upstream flow-deformation technique, which is discussed in the work by Wassermann & Kloker (2002) and the former effect can also be used for flow-control applications. In principle, after detecting a vortex, an opposite vorticity can be employed to damp it. However, this task is certainly not trivial, as experiments (Litvinenko *et al.* 2003) and computations (Messing & Kloker 2000) demonstrate, and the control scheme also requires an optimization. Meanwhile, this is an additional possibility to the technique of upstream flow deformation.

Concerning the factors affecting the preferred secondary instability mode, it is expected that the ratio of the vortex width to the vortex height is the governing parameter. The vortex height in our case can be defined as, for example, the distance
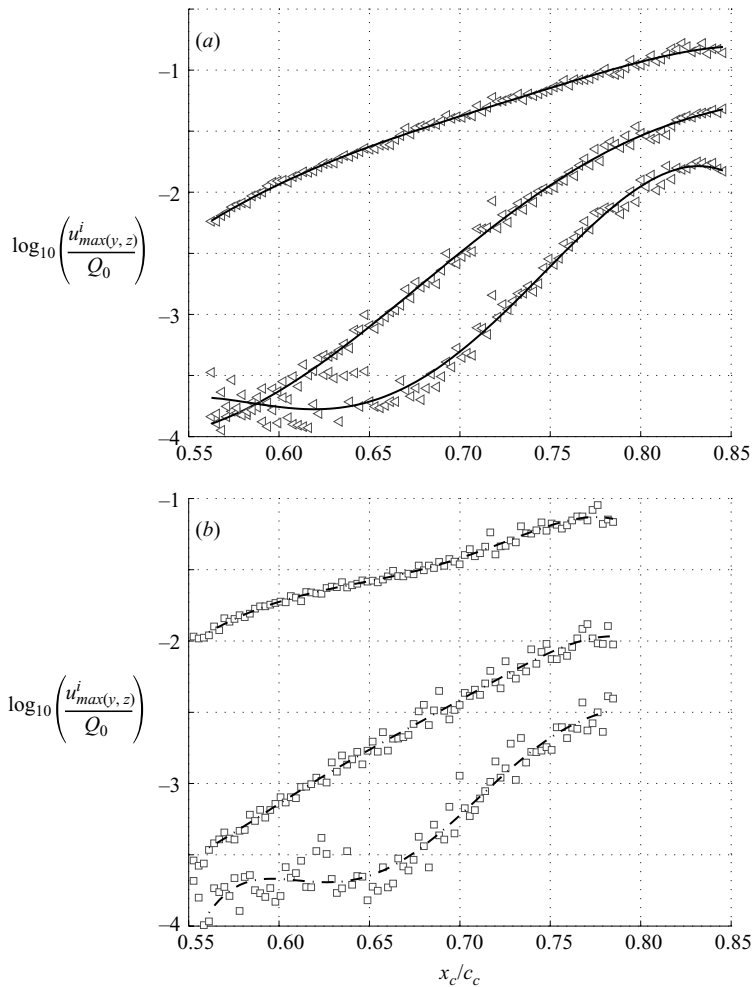
FIGURE 21. Downstream development of first, second and third (from top to bottom in each graph) harmonics of secondary instability at their maximum values. (*a*) Case A, (*b*) Case B, lines are fitting polynomials.

from the wall to the point of the highest spanwise gradient of streamwise velocity, similarly to Wassermann & Kloker (2002). In our experiments, we found the vortex height to be about 3θ and 4θ in Case A and Case B, respectively. The vortex width can be defined as the distance between the nearest strongest maxima and minima of the gradient. This value is approximately 12θ and 27θ in the above cases. Therefore, the vortex packet which favours the 'y' mode of secondary instability has about a 1.5 times larger width-to-height ratio. An analysis was also performed of results by Wassermann & Kloker (2002) and it was found that where the 'z' instability modes were observed, the ratio of the vortex width to height is approximately unity, while in their Case 4B, where the 'y' instability mode is generated, the ratio is nearly 1.4. Thus, in a very similar way, the width-to-height ratio is defining the secondary instability as was observed in two-dimensional flows. This could be a possible reason for explaining why in some swept-wing transition experiments only 'y' type modes of secondary instability are observed and in others 'z' type modes are prevailing.

4. Conclusions

As a result of the current study, experimental data on secondary instability in a swept-wing boundary layer including characteristics of the base flow, primary streamwise vortices and secondary perturbations was obtained. Detailed measurements were performed with both stationary vortices and secondary instabilities excited in a controlled manner. The characteristics of secondary instability obtained include phase information, growth rates and the development of nonlinear harmonics.

Wassermann & Kloker (2002) clearly demonstrated that packets of stationary crossflow vortices are most dangerous with respect to the secondary instability onset. In experiments under natural conditions, the stationary-flow modulation also appears non-uniform, testifying to the presence of packets rather than to single-mode stationary vortices. Also, the experiments revealed that the secondary instabilities develop within the packets of highest amplitude in an independent manner from the surrounding vortices. These packets represent the flow modulations of an alternating weak/strong vortex pattern, which is different from the modulation by regular vortices having a medium/medium pattern. It is expected that the character of the vortex packets, being composed from several spanwise modes, allows these disturbances to induce stronger distortions of the flow, namely stronger spanwise gradients. In this sense, the vortex packet is similar to a saturated single-mode vortex, which also induces higher gradients. As our study demonstrates, the saturation of primary stationary modes is of itself not a major necessity.

It can be assumed that under natural conditions of transition, such packets in a boundary layer may be triggered by some localized space forcing, for example, by isolated elements of surface roughness. In the present case, these conditions were modelled. It was found that in a three-dimensional boundary layer, two types of stationary vortex packets are possible, which can be named fundamental. These two packets represent localized vortices of different directions of rotation. It seems that the most important differences of these two vortex packets are in the different signs of the strongest gradient $\partial U/\partial z$, the different modification of the crossflow velocity which either increases or decreases the existing crossflow and, finally, in the different width of the low-speed streak formed.

Packets of positively rotating vortical disturbances (clockwise for the positive base crossflow) are found to be more favourable for the secondary instability. In our case, these packets lead to the quickest flow breakdown, which is associated with the development of the 'z' mode of secondary instability. The topology of negatively rotating packets is such that they can be more stable and can favour development of the 'y' mode of secondary instability. An important observation is that the localized suction generates a vortex packet of high instability similar to the positively rotating vortex generated from the roughness element. Thus, when the localized suction is used for flow-control purposes on the swept wing, this effect should be considered. On the other hand, since the disturbances developed owing to suction are very close to the disturbances derived from the roughness elements, the roughness elements might be used for the flow control instead of suction. It was also observed that the nonlinear interaction of the stationary disturbances having the form of a pair of counter-rotating vortices (as those created by two sides of a roughness element) leads to their mutual damping and, in principle, this effect can be used in flow-control strategies. However, it does require optimization. It was also demonstrated that excitation of a stationary mode of very high wavelength is hardly possible since the vortex generator of large span produces a pair of isolated vortices (vortex packets).

Overall, we found that 'z' type modes of secondary instability, which develop in extreme spanwise gradients of streamwise velocity, seem to grow faster than 'y' type modes, which were observed further from the wall within the low-momentum area of the vortex. The location of both instability modes is found to correlate well with the inflection of the spanwise velocity component. Analysis of these results and results of other available works suggests that, in general, the inflection of the crossflow velocity component favours secondary instability onset around this location. The type of distortion of spanwise velocity component (promotion or reduction) seems not to affect secondary instability much, while the added disturbance velocity moves the inflection point of the crossflow velocity component with respect to the wall.

The phase velocity vector of secondary instabilities is found significantly angled to the external flow streamline and to the primary stationary vortex (approximately $50°$–$70°$). The obliqueness might increase further when nonlinear interactions occur between the secondary disturbance and the mean flow. The secondary disturbances are almost non-dispersive during the linear and weakly nonlinear stages of development. As a result the secondary perturbations keep at a constant location relative to the primary vortex and within the vortex. Further, when nonlinear interactions take place, they result in a significant spreading out of perturbations in the direction of the crossflow and this nonlinear process should be a subject for further investigations.

An observation was made that the ratio of the vortex width to the vortex height might be a determining factor for the selection of the secondary instability mode. The vortex packet, which favours a 'y' mode of secondary instability has about 1.5 times larger width-to-height ratio than the vortex packet with a 'z' mode of secondary instability. This is might be a possible explanation of the fact that in different experiments, different types of secondary instabilities are observed as being dominant.

The threshold condition for the secondary instability in terms of the average between the maximum and minimum of the stationary disturbance of the streamwise velocity is about 7–10 %. Within the primary vortex of the amplitude below the threshold value, the secondary instabilities are found to be nearly neutrally stable.

As secondary instabilities develop, nonlinear interactions occur and the nonlinear development of the travelling secondary instabilities is found to be associated with the production of higher harmonics of the secondary instability frequency.

REFERENCES

ANDERSSON, P., BRANDT, L., BOTTARO, A. & HENNINGSON, D. 2001 On the breakdown of boundary layer streaks. *J. Fluid Mech.* **428**, 29–60.

ASAI, M., MINAGAWA, M. & NISHIOKA, M. 2002 The instability and breakdown of a near-wall low-speed streak. *J. Fluid Mech.* **455**, 289–314.

BOIKO, A., GREK, G., DOVGAL, A. & KOZLOV, V. 2002 *The Origin of Turbulence in Near-Wall Flows.* Springer.

BOIKO, A. V., KOZLOV, V. V., SOVA, V. A. & SCHERBAKOV, V. A. 2000 Generation of streamwise structures in a boundary layer of a swept wing and their secondary instability. *Thermophys. Aeromech.* **7**, 25–35.

BOIKO, A. V., KOZLOV, V. V., SYZRANTSEV, V. V. & SCHERBAKOV, V. A. 1995*a* Experimental investigation of high frequency secondary disturbances in swept wing boundary layer. *Appl. Mech. Tech. Phys.* **36** (3), 74–83, in Russian.

BOIKO, A. V., KOZLOV, V. V., SYZRANTSEV, V. V. & SCHERBAKOV, V. A. 1995*b* Experimental investigation of the transition process at an isolated stationary disturbance in swept wing boundary layer. *Appl. Mech. Tech. Phys.* **36** (1), 72–84, in Russian.

BOIKO, A. V., KOZLOV, V. V., SYZRANTSEV, V. V. & SCHERBAKOV, V. A. 1997 A study of the influence of internal structure of a streamwise vortex on the development of traveling disturbances inside it. *Thermophys. Aeromech.* **4**, 343–354.

BOIKO, A. V., KOZLOV, V. V., SYZRANTSEV, V. V. & SCHERBAKOV, V. A. 1998 Active control over secondary instability in a three-dimensional boundary layer. *Thermophys. Aeromech.* **6**, 167–178.

BOTTARO, A. & KLINGMANN, B. G. B. 1996 On the linear breakdown of Görtler vortices. *Eur. J. Mech.* B/*Fluids* **15**, 301–330.

BRANDT, L. & HENNINGSON, D. 2002 Transition of streamwise streaks in zero-pressure-gradient boundary layers. *J. Fluid Mech.* **472**, 229–261.

CHANG, H., CHERNORAY, V. & LÖFDAHL, L. 2003 Breakdown of near-wall streaks in straight wing boundary layer. In *Svenska mekanikdagar*, p. 136. Göteborg, Sweden.

CHERNORAY, V., KOZLOV, V., PRATT, P. & LÖFDAHL, L. 2005 Hot wire visualizations of breakdown to turbulence in complex flows. In *Proc. EUCASS Conf. Moscow, Russia*, 2005, pp. 2.11–2.12.

CORBETT, P. & BOTTARO, A. 2001 Optimal linear growth in swept boundary layers. *J. Fluid Mech.* **435**, 1–23.

DEYHLE, H. & BIPPES, H. 1996 Disturbance growth in an unstable three-dimensional boundary layer and its dependence on environmental conditions. *J. Fluid Mech.* **316**, 73–113.

ELOFSSON, P., KAWAKAMI, M. & ALFREDSSON, P. 1999 Experiments on the stability of streamwise streaks in plane Poiseuille flow. *Phys. Fluids* **11**, 915–930.

FISCHER, T. M. & DALLMANN, U. 1991 Primary and secondary stability analysis of a three-dimensional boundary-layer flow. *Phys. Fluids* A **3**, 2378–2391.

HAYNES, T. & REED, H. 1997 Numerical simulation of swept-wing vortices using nonlinear parabolized stability equations. *SAE Paper* 971479.

HAYNES, T. & REED, H. 2000 Simulation of swept-wing vortices using nonlinear parabolized stability equations. *J. Fluid Mech.* **405**, 325–349.

HÖGBERG, M. & HENNINGSON, D. 1998 Secondary instability of crossflow vortices in Falkner–Skan–Cooke boundary layers. *J. Fluid Mech.* **368**, 339–357.

ITO, A. 1988 Breakdown structure of longitudinal vortices along a concave wall; on the relation of horseshoe-type vortices and fluctuating flows. *J. Japan Soc. Aero. Space Sci.* **36**, 274–279.

JANKE, E. & BALAKUMAR, P. 2000 On the secondary instability of three-dimensional boundary layers. *Theor. Comput. Fluid Dyn.* **14**, 167–194.

KAWAKAMI, M., KOHAMA, Y. & OKUTSU, M. 1999 Stability characteristics of stationary crossflow vortices in three-dimensional boundary layer. *AIAA Paper* 99-0811.

KOCH, W. 2002 On the spatio-temporal stability of primary and secondary crossflow vortices in a three-dimensional boundary layer. *J. Fluid Mech.* **456**, 85–111.

KOCH, W., BERTOLOTTI, F., STOLTE, A. & HEIN, S. 2000 Nonlinear equilibrium solutions in a three-dimensional boundary layer and their secondary instability. *J. Fluid Mech.* **406**, 131–174.

KOHAMA, Y. 1987 Some expectation on the mechanism of cross-flow instability in a swept-wing flow. *Acta Mech.* **66**, 21–38.

KOHAMA, Y., ONODERA, T. & EGAMI, Y. 1996 Design and control of crossflow instability field. In *IUTAM Symp. on Nonlinear Instability and Transition in Three-Dimensional Boundary Layers* (ed. P. Duck & P. Hall), Manchester, UK. pp. 147–156. Kluwer.

KOHAMA, Y., SARIC, W. & HOOS, W. 1991 A high-frequency, secondary instability of cross-flow vortices, that leads to transition. In *Proc. RAS Conf. on Boundary-Layer and Control*, pp. 4.1–4.13. Cambridge, UK.

KOHAMA, Y. P., ALFREDSSON, P. H., EGAMI, Y. & KAWAKAMI, M. 2000 Turbulent energy production mechanism in general boundary layer transition. In *Laminar-Turbulent Transition. Proc. IUTAM Symp. 1999, Sedona, AZ, USA* (ed. H. Fasel & W. Saric), pp. 205–210. Springer.

KOZLOV, V., CHERNORAY, V., LITVINENKO, Y. & LÖFDAHL, L. 2004 Breakdown of a streak via development of varicose secondary mode on the straight wing with pressure gradient. In *Adv. in Turbulence X, Proc. X European Turbulence Conf. Trondheim, Norway* (ed. H. Andersson & P.-A. Krogstad), pp. 77–82. CIMNE, Barcelona.

KOZLOV, V., SOVA, V. & SHCHERBAKOV, V. 2001 Experimental investigation of the development of secondary perturbations on a swept wing. *Fluid Dyn.* **36**, 909–914.

LITVINENKO, Y., KOZLOV, V., CHERNORAY, V. & LÖFDAHL, L. 2003 Control of cross-flow instability on a swept wing by suction. *Thermophysics and Aeromechanics* **10** (4), 541–548.

MALIK, M., LI, F. & CHANG, C.-L. 1994 Crossflow disturbances in three-dimensional boundary layers: nonlinear development, wave interaction and secondary instability. *J. Fluid Mech.* **268**, 1–36.

MALIK, M., LI, F., CHOUDHARI, M. & CHANG, C.-L. 1999 Secondary instability of crossflow vortices and swept-wing boundary-layer transition. *J. Fluid Mech.* **399**, 85–115.

MATSSON, O. & ALFREDSSON, P. 1990 Curvature- and rotation-induced instabilities in channel flow. *J. Fluid Mech.* **210**, 537–563.

MATSUBARA, M. & ALFREDSSON, P. 2001 Disturbance growth in boundary layers subjected to free-stream turbulence. *J. Fluid Mech.* **430**, 149–168.

MESSING, R. & KLOKER, M. 2000 Effect of suction through arrays of holes in a 3-d boundary layer investigated by spatial direct numerical simulation. In *Laminar–Turbulent Transition. Proc. IUTAM Symp. 1999, Sedona, AZ, USA* (ed. H. Fasel & W. Saric), p. 136. Springer.

NITSCHKE-KOWSKY, P. & BIPPES, H. 1988 Instability and transition of a three-dimensional boundary layer on a swept flat plate. *Phys. Fluids* **31**, 786–795.

POLL, D. I. A. 1979 Transition in the infinite swept attachment line boundary layer. *Aeronaut. Q.* **30**, 607–629.

POLL, D. I. A. 1985 Some observations on the transition process on the windward face of a long yawed cylinder. *J. Fluid Mech.* **150**, 329–356.

ROGET, C., BRAZIER, J. P., COUSTEIX, J. & MAUSS, J. 1998 A contribution to the physical analysis of separated flows past three-dimensional humps. *Eur. J. Mech.* B/*Fluids* **17**, 307–329.

SARIC, W., REED, H. & WHITE, E. 2003 Stability and transition of three-dimensional boundary layers. *Annu. Rev. Fluid Mech.* **35**, 413–440.

SCHOPPA, W. & HUSSAIN, F. 2002 Coherent structure generation in near-wall turbulence. *J. Fluid Mech.* **453**, 57–108.

SKOTE, M., HARITONIDIS, J. H. & HENNINGSON, D. S. 2002 Varicose instabilities in turbulent boundary layers. *Phys. Fluids* **14**, 2309–2323.

WASSERMANN, P. & KLOKER, M. 2002 Mechanisms and passive control of crossflow-vortex-induced transition in a three-dimensional boundary layer. *J. Fluid Mech.* **456**, 49–84.

WHITE, E. & SARIC, W. 2005 Secondary instability of crossflow vortices. *J. Fluid Mech.* **525**, 275–308.

WHITE, E., SARIC, W., GLADDEN, R. & GABET, P. 2001 Stages of swept-wing transition. *AIAA Paper* 2001-0271.